Experimental and theoretical studies for the structure of copper single-atom catalyst

銅単原子触媒の構造に関する実験的および理論的研究

Chorong KIM

金　チョロン

Division of Quantum Science and Engineering,

Graduate School of Engineering, Hokkaido University

March 2024

Abstract

Monodispersed atom on oxide carriers exhibits unique catalytic activity and are called single-atom catalysts (SACs). Due to its high catalytic activity and the cost-saving effect of metals, it has recently attracted attention. A normal SAC is obtained by immobilizing a metal species on the oxide surface via surface hydroxyl groups or linker molecules strongly interacting with both the metal species and the substrate. As a result, the geometric and electronic properties of single atoms are mainly determined by local coordination environments around single atoms. Therefore, it is important to determine the local coordination environment around the single atom to understand catalytic properties. In normal SACs, metal species are highly dispersed on polycrystalline oxide powders having microporous structures, so it is difficult to determine the local coordination environment around the single atom. Therefore, I tried to achieve high atomic dispersion of copper by pre-modifying the surface with organic linker molecules using a single crystal oxide that is easy to define monatomic structure. The polarization total reflection fluorescence X-ray absorption microstructure (PTRF-XAFS) indicates a single atom structure and determines the local coordination environment around the monatomic by using it in combination with density functional theory (DFT) calculation. In this study, I proposed atomic dispersion determinants and fatal defects by the PTRF-XAFS method, which is the only method to stereoscopically determine highly dispersed

atomic structures on a single crystal surface.

This dissertation consists of six chapters.

Chapter 1 is an overview, and the advantages of single-atom catalysts are shown after describing the problems of heterogeneous catalysts in general catalytic reactions.

Chapter 2 describes experimental and theoretical methods for determining the structure of the catalyst obtained. This chapter describes PTRF-XAFS measurements and analysis methods performed mainly for structural analysis and details the theoretical methodology using DFT.

Chapter 3 presents the preparation of copper atoms on pre-modified TiO_2(110) surfaces and their structural determination. A PTRF-XAFS method of a copper chemical species sandwiched between an NH_2 group in anthranilic acid and a hydroxyl group of TiO_2(110) is measured by depositing copper on TiO_2(110) immersed in anthranilic acid to show atomic dispersion. A local coordination environment around a copper single atom is determined three-dimensionally from simulation by an FEFF code, and its model structure is proposed.

In Chapter 4, structural optimization of copper SACs was performed in DFT calculations to obtain the structure and electronic state of the entire TiO_2(110) surface from local structures obtained by PTRF-XAFS. It was found that the structure obtained in the experiment could not reproduce the structure of copper SAC from DFT calculation. In the optimized structure of copper SAC, anthranilic acid is inclined to the TiO_2(110)

surface, and the local coordination structure of copper shows a more linear structure with respect to the TiO_2(110) surface.

Chapter 5 reconstructed the structure of copper SAC based on the structure optimized from DFT calculations and compared the new model structure with PTRF-XAFS results. As a result, it is shown that PTRF-XAFS of copper SAC can be reproduced with a structure obtained from DFT calculation. It showed that there is a structure that cannot be determined by PTRF-XAFS, the only method that can measure highly dispersed metal species in three different directions on the single crystal surface, so it is essential to use it with theoretical discussion. In addition, the scope of application of atomic dispersion determination was proposed compared with other SAC structures.

In the final Chapter 6 summarizes this thesis.

Preface

The study in this dissertation has been carried out under the direction of Professor Kiyotaka Asakura from April 2020 to March 2024 at the Division of Quantum Science and Engineering, Graduate School of Engineering, Hokkaido University.

The author is greatly indebted to Professor Kiyotaka Asakura for his significant guidance, continuous encouragement, and fruitful suggestions. The author wishes to express his sincere gratitude to Professor Satoru Takakusagi for his deep kindness and dedicated support throughout this work.

The author would like to thank the past, and present secretaries, technicians, undergraduate/graduate students, post-doctoral fellows, and staff of the Asakura laboratory for their encouragement and friendship during my laboratory life. The author wishes to especially thank Dr. Daiki Kido, Dr. Bang Lu, and Ms. Kaiyue Dong for their friendly support and competition.

Finally, the author wishes to offer special thanks to her family, Dr. Tomohiro Fukushima, Mr. Jun Fukushima, and my family in Korea and Nagoya, for their all patience, financial support, and endearing dedication.

Chorong Kim

Catalyst Surface Research Laboratory

Division of Quantum Science and Engineering

Graduate School of Engineering, Hokkaido University

Contents

Chapter 1

General introduction

Why Surface is important?

Since the 1960s, the study of solid surfaces has experienced significant growth due to an increasing awareness of their importance. Surfaces, serving as unique defects in the solid state, disrupt the perfect periodicity of solids, leading to structural changes and localized electronic and vibrational states. This disruption is academically intriguing and relevant for low-dimensional structures in semiconductor devices.

Surface studies are primarily motivated by heterogeneous catalysis, aiming to understand enhanced chemical interactions on solid catalysts. This involves identifying modifications upon adsorption, exploring intermediate species formation, discerning rate-limiting steps, determining active sites, and understanding catalyst material variations. Surface studies contribute not only to theoretical understanding but also to practical advancements in semiconductor technology and catalysis. Despite the potential for developing improved catalysts, especially with precious metals like platinum, exploring microscopic processes poses formidable challenges. To address these challenges, a technique involves studying simplified versions of catalytic problems by examining flat,

low Miller index faces of single crystals in an Ultra-High-Vacuum (UHV) environment. The focus is on characterizing surfaces, adsorption, and reaction processes in detail to ensure well-defined conditions. Despite appearing distant from applied catalytic problems, this approach has proven valuable since the early 1980s, providing insights into simple catalytic reactions at a microscopic level. Researchers have successfully expanded to more complex problems, demonstrating the method's potential in unraveling catalytic intricacies.

Another significant research area focuses on comprehending material corrosion and defects on surfaces. Analyzing the composition of the top atomic layers of a fractured or corroded surface yields valuable insights. By employing surface-specific analytical techniques and controlled removal of atomic layers, researchers can generate depth profiles of surface and subsurface composition. This approach enhances our understanding of surface structure at the atomic and molecular levels, guiding practical issue mitigation. For instance, examining actual semiconductor devices with structural rearrangements compared to the bulk structure reveals inherent challenges connected to the modeling approach used in catalytic research. Techniques such as high-energy electron diffraction and Scanning Tunneling Microscopy (STM) have played a crucial role in understanding complex reconstructions, particularly in basic surface analysis. Therefore, gaining a comprehensive understanding of surfaces and surface analysis techniques is essential for designing new materials in the realm of atomic engineering.

Single-atom catalyst (SAC)

Most of the catalysts used in our lives are powders. The powder catalyst has various surfaces exposed, and the shape, size, and direction of the exposed crystal surface are different. Since powdery catalysts have so many parameters that determine the structure, it is difficult to analyze and clarify which parameters affect catalyst activity. Therefore, when studying the activity of the supported metal catalyst (called single atom catalyst, SAC), a model catalyst whose surface structure is specified is often used. For example, by carrying metal atoms on a carrier having a specified surface structure such as a single crystal, parameters such as particle shape and crystalline surface direction are eliminated, and the activity of the supported metal catalyst on a specific surface can be studied at pinpoint. In particular, the surface of titanium oxide TiO_2 (110) described later has been studied very much, and since the surface structure is well known, it is often used as a carrier for model-supported metal catalysts. In the supported metal catalyst, metal nanoparticles are supported on surfaces having relatively high strength and large surface areas. Because the metal is dispersed into nanoparticles having a large specific surface area, activity as a catalyst of the metal is improved and cost can be suppressed. A metal-carrying oxide has a wide variety of applications and is used not only for catalysts but also for gas sensors, electronic materials, and magnetic materials. To develop a next generation supported metal catalyst, metal atoms/small metal particles of less than 1 nm need to be highly dispersed on the carrier. However, metals have low adsorption energy

and diffusion barriers, so they easily aggregate when trying to vaporize nanoparticles in a vacuum. It can be said that technology to control the size of metal nanoparticles at the molecular and atomic levels is essential for the future development of supported metal catalysts.

It is difficult to create monatomic Cu on a TiO_2(110) surface by Cu evaporation onto the TiO_2 surface. Cu is easily aggregated to form clusters. This is due to the small stabilization energy and/or the small activation energy for the metal diffusion, suggesting the strength of the Cu bridging oxygen bond is not sufficient to fix the Cu atom. Therefore, organometallic Cu had to be used to stabilize the surface species in the presence of suitable ligands.[1]

Surface premodification method

Grafting methods typically require the preparation of organometallic compounds in advance, although these compounds are often unstable in air or at high temperatures. However, if the oxide support surface is premodified with an organic ligand that strongly anchors to a metal atom through a covalent bond, then a well-defined atomic metal species can be obtained without the need for organometallic compounds. W. Chun *et al.* have prepared an atomically dispersed Cu–thiophene compound with the Cu–S bond simply by vacuum deposition of Cu on a TiO_2(110) surface that was premodified with thiophene carboxylic acid (TCA) in which the carboxylic group acted as a binding part to the

TiO_2 substrate.[2] This preparation method referred to as the surface premodification method, allows for the use of various organic compounds for premodification, enabling selective fine-tuning of surface metal structures. As another example of fine-tuning, atomically dispersed Cu species using mercaptobenzoic acid (MBA) isomers (*o*-MBA, *m*-MBA, and *p*-MBA) containing different mercapto group distances from the surface, which might control the location of Cu.[3] Cu was positioned almost linear S–Cu–O (lattice oxygen of TiO_2) surface compounds on the three MBA-modified TiO_2(110) surfaces; however, the orientation of the Cu species on the *o*- and *m*-MBA-modified TiO_2(110) surfaces (40–45 inclined from the surface normal) was different from that on the *p*-MBA-modified TiO_2(110) surface (60 from the surface normal). These results suggest that the selection of an organic linker molecule deposited on a single crystal oxide surface would enable fine-tuning of the orientation and configuration of active metal structures. Moreover, catalytic activities of the Cu species are expected to be varied with their configurations on the TiO_2(110).

Structure determination by PTRF-XAFS

XAFS is a modulation appearing around and above the X-ray absorption edge and its origin is the interference between outgoing photoelectrons from the X-ray absorption and scattered electrons by the surrounding atoms. The oscillatory feature of XAFS provides information about the bond distance and coordination number in high

precision. Since the XAFS does not require a long-range order, the structure of metal species on powdery oxide supports is efficiently studied by this technique.[4] If the XAFS can be applied to nanoparticles dispersed on a single crystal oxide as a model of real supported catalysts, we will have definite information about the structure of supported nanoparticles and the metal–support interaction. In addition, the XAFS oscillation, χ(k), has the following polarization dependence on the angle, θ_j, between the X-ray electric vector (polarization direction) and *j*th bond direction in the K-absorption edge[5] where χ(k) represents the XAFS oscillation of the *j*th bond.

$$\chi_{obs}(k) = \sum_i 3\cos^2\theta_i \cdot \chi_i(k) \qquad \text{(Equation 1-1)}$$

Furthermore, XAFS measurement with the various polarization directions such as [001], $[1\bar{1}0]$, and [110] directions can be obtained from the three-dimensional (3D) structural information. Moreover, when the polarization is directed toward the substrate, the metal–support interaction can be more selectively detected. Another challenge in applying XAFS to a single crystal system is the low concentration of metal nanoparticles and the high background noise from the support. A single crystal oxide surface has typically a few cm^2 and the amount of metal species on it is only around 10^{-10} mol. Such difficulty can be solved by the combination of the total reflection and fluorescence detection mode of XAFS. The fluorescence method gives us the XAFS signal of the dilute system, and the probability of the fluorescence decay process of a core hole is larger than that of the Auger decay process in the hard X-ray region. Consequently, the XAFS signal

of the metal species at the surface can be detected as small as 10^{13} cm^{-2}.[6] This technique is called polarization-dependent total reflection fluorescence X-ray absorption fine structure (PTRF-XAFS).[7] Furthermore, PTRF-XAFS can be performed in situ or operando measure, providing information about the metal oxidation state, electronic properties, and bonding geometry obtained from the XANES region. The analysis of the EXAFS region offers insights into the absorbing atom, including the types, number, and bond distances of the nearest neighbor atom within approximately ~5 Å.[8-10] However, XAFS has a particular limitation. The most significant challenge lies in the fact that the structure of metal species is not determined directly via EXAFS to measure data fit with an entire structural model. Structural determination via EXAFS is thus an inverse problem, subject to subjective interpretations to ascertain whether a proposed structural model is statistically valid and distinguishable from other structures. Consequentially, there is always the potential for ambiguity in conclusions regarding the structures of metal species in a sample.

Modeling single-atom catalyst by DFT calculation

Atomic-scale details regarding the active sites and reaction mechanisms are proposed primarily based on density functional theory (DFT) calculations. Periodic slab calculations based on a low-index facet of the support material are used, which may or may not appear on the powder catalyst. A suitable adsorption site for the metal adatom is

then commonly selected based on strong binding energy relative to other possible sites in DFT with some guidance from the experiment. In the surface-science approach, a single-crystalline sample exhibiting a low-index surface orientation is prepared under UHV conditions (typically by Ar^+ sputtering and high-temperature annealing) until it is free of contamination such as OH groups and carbon. In this state, the system resembles an experimental analog of that simulated by periodic slab calculations. Crucially, the atomic-scale structure of the surface has been determined with sub-Angstrom precision for several common support materials such as titanium oxide[11], cerium oxide[12], and iron oxide[13]. While such model surfaces necessarily lack some of the complexity of applied SAC systems, they can serve as a solid basis for experimental studies of SAC mechanisms and as a benchmark for the theoretical approach used in high surface area catalytic studies.

Aim of thesis

Single-atom catalysts can be achieved by grafting a metal complex onto an oxide surface through a reaction with OH groups or by anchoring a metal species with a linker molecule that strongly interacts with both the metal and support. Although the structures and oxidation states of surface metal species can be precisely controlled at the atomic level, determining the three-dimensional structure, including orientation, coordination, and configuration relative to the support surface, poses challenges. The use of PTRF-XAFS measurement emerges as a promising method for surface observation. Additionally,

the careful selection of a premodified molecule deposited on a single crystal oxide surface allows for the fine-tuning of the orientation and configuration of active metal structures. To compensate for the experimental limitations, theoretical structure determination is performed in parallel to make a precisely defined structure of SAC.

This thesis focuses on the structural determination of Cu atomic catalysts premodified with organic ligands. The aim is to explore and understand the intricate details of the surface structures, providing insights into how the orientation and configuration of active metal species, particularly Cu, influence catalytic activities on the TiO_2(110) surface. This research contributes to advancing our understanding of the design and optimization of immobilized metal species, paving the way for enhanced catalytic applications in research fields.

Reference

1 Y. Tanizawa, W.-J. Chun, T. Shido, K. Asakura, Y. Iwasawa, *Journal of Synchrotron Radiation* **2001**, *8*, 508.

2 W.-J. Chun, Y. Koike, K. Ijima, K. Fujikawa, H. Ashima, M. Nomura, Y. Iwasawa, K. Asakura, *Chemical Physics Letters* **2007**, *433*, 345.

3 S. Takakusagi, H. Nojima, H. Ariga, H. Uehara, K. Miyazaki, W. J. Chun, Y. Iwasawa, K. Asakura, *Phys Chem Chem Phys* **2013**, *15*, 14080.

4 Y. Iwasawa, *X-Ray Absorption Fine Structure for Catalysts and Surfaces*.

5 M. Shirai, K. Asakura, Y. Iwasawa, *Japanese Journal of Applied Physics* **1993**, *32*, 413.

6 Y. Koike, K. Ijima, W. J. Chun, H. Ashima, T. Yamamoto, K. Fujikawa, S. Suzuki, Y. Iwasawa, M. Nomura, K. Asakura, *Chemical Physics Letters* **2006**, *421*, 27.

7 K. Asakura, in *Catalysis*, ed. by J. J. Spivey, M. Gupta, The Royal Society of Chemistry, **2012**, *24*.

8 J. J. Rehr, J. J. Kas, M. P. Prange, A. P. Sorini, Y. Takimoto, F. Vila, *Comptes Rendus Physique* **2009**, *10*, 548.

9 S. Calvin, *XAFS for Everyone*. CRC press, **2013**.

10 M. Newville, *Reviews in Mineralogy and Geochemistry* **2014**, *78*, 33.

11 U. Diebold, *Surface Science Reports* **2003**, *48*, 53.

12 Y. Jiang, J. B. Adams, M. van Schilfgaarde, *The Journal of Chemical Physics*

2005, *123*,

13 J. Lin, B. Qiao, N. Li, L. Li, X. Sun, J. Liu, X. Wang, T. Zhang, *Chemical Communications* **2015**, *51*, 7911.

Chapter 2

Experimental description

I introduced in detail to understand used materials with experimental descriptions and explained several surface characterization techniques in this chapter.

Materials

Rutile TiO_2(110) surface

Rutile TiO_2(110) stands out as one of the most extensively studied systems in surface science.[1, 2] Along the [001] direction, there are protruding oxygen atoms referred to as "bridging oxygen atoms". The troughs between the rows of bridging oxygen atoms (O_{2c}) are where 5-fold-coordinated titanium (Ti_{5c}) and in-plane oxygen atoms are located (Figure 2-1). This is partly because single-crystal samples of high quality are inexpensive and widely available and partly because UHV preparation can be easily achieved by in situ cycles of inert gas sputtering followed by annealing. This treatment results in a slight reduction of the sample, which is sufficient to allow experiments based on electron transfer (STM, XPS, etc.).[3] The structure of the as-prepared surface is precisely known from quantitative structural techniques (SXRD/LEED)[4, 5], and the results agree with DFT[6]

calculations and fit well with the results of scanning probe studies[7]. Interestingly, the contrast observed in STM is reversed from the topography, the low-lying Ti_{5c} atoms are imaged bright, and the protruding bridging O_{2c} rows are imaged dark (Figure 2-2a and 2-2b).[1,7] This is related to the electronic structure and the fact that the Ti atoms have electronic states close to the Fermi level. The newest generation of scanning probe instruments allows simultaneous imaging by STM and noncontact AFM, allowing one to image both the atomic and the electronic structures of the surface. Due to the reduction of the sample, surface oxygen vacancies (VO) are common defects. They are imaged as bright protrusions in the dark O_{2c} rows in STM and as missing atoms in the O_{2c} rows in nc-AFM (Figure 2-2a and 2-2c). The reduced surface is often denoted r-TiO_2(110). TiO_2(110) has been the importance of VO as active sites for both chemical reactions and the nucleation of metal nanoparticles.[8] For example, water molecules react with the oxygen vacancies creating two surface hydroxyl groups, a pair of H atoms adsorbed at the O_{2c} rows. This reaction is highly efficient, and the residual water in a UHV environment is sufficient to fill all of the VO sites over several hours. When saturation exposure to water creates a partially hydroxylated surface, it is often referred to as h-TiO_2(110). Similarly, exposing the r-TiO_2(110) surface to very small amounts of molecular oxygen results in the repair of the vacancy and the adsorption of an O atom atop the Ti5c rows. The resulting surface is then termed o-TiO_2(110). It is important to note that realistic catalytic environments will thus not have surface VO present in an

appreciable number.

o-anthranilic acid (o-AA)

Anthranilic acid is an aromatic acid with the formula $C_6H_4(NH_2)(CO_2H)$. The molecule consists of a benzene ring, ortho-substituted with a carboxylic acid and an amine (Figure 2-3). This molecule is what I use because the carboxylic acid group-containing anthranilic acid can be stable and anchored to the TiO_2 surface binding to the Ti_{5c}. In addition, the amine functional group can interact with the dispersed metal species by the free rotation of the benzene ring. Consequently, the metal diffusion is interfered and difficult to aggregate each other.

Clean surface of TiO_2(110)

In this experiment, an Nb-doped rutile TiO_2(110) single crystal substrate (Nb: 0.05 wt.%, 20×20×1 mm) was used. To prepare a clean TiO_2 (110) substrate, several procedures were carried out before the experiment, as shown below.

1. The substrate was immersed in thermal royal water at 80 °C for one hour, and metal atoms adhering to the surface of the substrate were dissolved.
2. The substrate was then removed and washed eight times with ultrapure water. Then, the substrate was immersed in a Piranha solution, a mixture of sulfuric acid

and hydrogen peroxide water with a 3:1 ratio, for one hour. This treatment decomposes the organic compounds adhering to the surface of the substrate.

3. Following the Piranha solution treatment, the substrate was removed, washed eight times with ultrapure water, and dried with argon gas. This drying process prevents the concentration of hydrofluoric acid from decreasing when the substrate is subsequently immersed in hydrofluoric acid.
4. The substrate was immersed in 10% hydrofluoric acid for 10 minutes to expose the new TiO_2 (110) surface. Hydrogen fluoride dissolves the TiO_2 surface through the following reaction:

$$TiO_2 + 6\ HF \rightarrow H_2[TiF_6] + 2H_2O \qquad \text{(Equation 2-1)}$$

The treated substrate was then washed eight times with ultrapure water and dried with argon gas. Additionally, since hydrofluoric acid has the property of dissolving glass, a Teflon beaker was used for this treatment.

5. The washed substrate was placed in an electric furnace and annealed at 700°C under the atmosphere. Annealing helps in recovering the steps and defects of the substrate.

Preparation of Cu/o-AA/TiO_2(110)

The cleaned surface was immersed in a 2 mM ethanol solution of *o*-AA (Wako Chemicals, Japan) for 24 hours to modify the TiO_2(110) surface with an *o*-AA monolayer.

The sample holder for arranging a substrate is previously immersed in acetone and ultrasonically cleaned. Then, the sample was introduced to the ultrahigh vacuum (UHV) PTRF-XAFS chamber and transferred into the preparation chamber to measure XPS, confirming that *o*-AA molecules were adsorbed on the substrate without contamination (Figure 2-4).[9] After that, the Cu was evaporated onto the *o*-AA/TiO_2(110) surface at room temperature by resistive heating of a tungsten filament wrapped with a Cu wire (99.999% purity, Nilaco Co., Japan) which source was controlled 4.6 Å and 0.85 V.

Cu coverage on the Cu/o-AA/TiO_2(110)

Cu coverage on the surface of *o*-AA/TiO_2(110) can be estimated by XPS analysis after Cu vapor deposition. The amounts of Cu were obtained in units of coverage θ (ML, monolayer=$5.2\times10^{14}/cm^2$), calculated by the following equation.

$$\theta = \frac{I_{Cu2p3/2}}{I_{Ti2p3/2}} \times \frac{\sigma_{Ti2p3/2}}{\sigma_{Cu2p3/2}} \times \frac{1}{1-\exp\left(-\frac{d_{Ti}}{\lambda_{Ti}}\right)} \qquad \text{(Equation 2-1)}$$

where I mean the intensity of each peak and σ is the photoionization cross-section.[10] d_{Ti} is the surface interval of Ti where d_{Ti}=0.325 nm. λ_{Ti} is an inelastic scattering average free stroke of TiO_2 which is obtained by reflection electron energy loss spectroscopy (REELS). This value changed by the energy of X-rays, AlKα (1486.6 eV) and $Ti2p_{3/2}$ peak (458.7 eV) have a difference of 1000 eV, therefore λ_{Ti}=1.5 nm is obtained.[11] A photoionization cross-section $\sigma_{Ti2p3/2}$ is 5.22 and $\sigma_{Cu2p3/2}$ is 16.73 when the cross-

section of C1s peak is set to 1. When the intensities of $Cu2p_{3/2}$ and $Ti2p_{3/2}$ peaks are obtained, the Cu coverage θ = 0.1 ML can be calculated.

N coverage on the Cu/o-AA/TiO_2(110)

N1s XPS spectra before and after Cu deposition were compared to verify the amounts of adsorbed *o*-AA molecule. The N coverage on *o*-AA/TiO_2(110) before Cu deposition was 0.4 ML, represented by the following equation similar to Equation 2-1.

$$\theta = \frac{I_{N1s}}{I_{Ti2p3/2}} \times \frac{\sigma_{Ti2p3/2}}{\sigma_{N1s}} \times \frac{1}{1-\exp\left(-\frac{d_{Ti}}{\lambda_{Ti}}\right)} \qquad \text{(Equation 2-2)}$$

where $\sigma_{N1s} = 1.8$

After Cu deposition, the N1s spectra was slight shift and broaden compared to the N1s spectrum of *o*-AA/TiO_2(110) before Cu deposition. Therefore, the peak fitting analysis was performed to confirm amounts of shifted N. The shifted N coverage θ = 0.1 ML. This value is closed to Cu coverage.

Measurements

Surface characterization techniques

Surface analysis requires the use of several analytical techniques including microscopic, spectroscopic, chemical, and physical methods that provide different types

of information about the surface of catalysts. The analysis is done to provide information about such characteristics as the chemical composition, the level of trace impurities, or the physical structure or appearance of the sampled region. Surface characterization techniques are often constrained by the information obtained from the measurements, but also by the conditions required for the analysis. For example, techniques that require a vacuum cannot be used for analyzing liquid or volatile chemicals. This limitation means that a given technique may have a limited range of applications. It is thus beneficial to employ more than one technique and combine results from several methods to get as much information as possible.

Among the criteria for selection of one or more of the techniques are: 1. The required depth of the surface analysis; 2. The required chemical information elemental or functional group; 3. Quantification of quantitative, semi-quantitative, or qualitative requirements; 4. Lateral resolution whether very small features or spots need to be detected; and 5. Is other information required, such as topographical information, about the sample surface?

Surface characterization of single-component systems has been extensively carried out on modified surfaces of oxide materials or adsorbed states of molecules. Such research has provided substantial information such as surface geometry and reconstruction, adsorbed states, and electrical properties of the surface. Based on this knowledge, I describe about surface characterization techniques I used for this thesis.

Atomic force microscope (AFM)

Atomic force microscope (AFM) employs a different approach than using the electron tunneling current to measure the tip-to-surface distance.[12] The schematic of AFM is shown in Figure 2-5. Instead, it gauges the force of interaction between a specimen surface and a sharp probe tip. The tip, typically a couple of micrometers long and less than 10 nm in diameter, is situated at the free end of a 100 to 200 mm long cantilever. As the tip approaches within a few angstroms of the specimen surface, repulsive van der Waals forces between the atoms on the tip and those on the specimen cause the cantilever to deflect or bend. A detector, such as the position-sensitive photodetector, measures the cantilever deflection as the tip is scanned over the specimen or the specimen is scanned under the tip. Utilizing a piezoelectric scanner, the tip is gently traced across the specimen, causing the cantilever to bend in response to changes in topography. The measured cantilever deflections enable a computer to generate a map of surface topography. The observed AFM image of the TiO_2(110) surface is shown in Figure 2-6.

AFM finds application in studying insulating, semiconducting, and electrically conducting materials. Most currently used AFMs detect the position of the cantilever using optical techniques. The position-sensitive photodetector can measure light displacements as small as 1 nm. The mechanical amplification resulting from the ratio of the path length between the cantilever and detector to the length of the cantilever itself allows the system to detect even 0.1-nm vertical movements of the cantilever tip. Various

methods exist for detecting cantilever deflection, including optical interference, using a scanning tunneling microscope tip, or employing piezoresistive detection (fabricating the cantilever from a piezoresistive material). A computer-generated map, developed from digital data obtained from closely spaced parallel profiles, can display the shape of a surface, showing both individual features and the general topography over an area.

The atomic force microscope was invented in 1986 by Binning *et al.* The first AFMs operated in contact mode[13]. In contact mode, the tip mounted onto the end of a flexible cantilever, raster scans the surface of the sample. The deflection of the cantilever due to tip-surface interaction reveals the sample surface. Samples can be analyzed in air, liquid, or vacuum. In liquids and vacuum systems, the absence of strong capillary forces due to a thin liquid film on all samples in the air can result in higher resolutions. In that mode, biological samples are difficult to scan using contact mode because they are often soft and weakly bound to the surface and therefore can be damaged easily. The non-contact mode was first introduced in 1987.[14] Developed to more accurately image soft biological samples, in non-contact mode the cantilever oscillates close to its resonant frequency at a small distance (1-10 nm) above the surface. Long-range attractive forces induce changes in the amplitude, frequency, and phase of the cantilever and maintain a constant distance during scanning. Because the forces on the sample are much lower than in contact mode, even the softest samples can be imaged without damage. Imaging in attractive mode is also possible. Tapping Mode was first introduced.[15] In this mode, the

cantilever oscillates at its resonant frequency, but unlike the non-contact mode, the cantilever gently taps the surface during scanning, greatly reducing damaging lateral forces. Tapping mode in fluids was first introduced in 1994 by the Hansma Lab.[16] In the first implementation of tapping mode in fluids, the sample, which sits on a piezoelectric scanner, oscillates up and down and taps the tip at the apex of each oscillation cycle. The amplitude of the piezoelectric is set manually at the beginning of the run, and the tapping force is held constant by a feedback loop. Smaller cantilevers were developed, allowing higher resolution and smaller scanning times. For biological samples, desirable cantilevers have a higher resonant frequency (and therefore a higher scanning speed) and a low spring constant. This is most easily achieved by decreasing the mass of a cantilever. Recently cantilevers have been fabricated on the order of 9-40 mm in length with resonant frequencies an order of magnitude higher than commercially available cantilevers. Improvements in instrumentation and understanding of the AFM have led to its wide use in many fields in engineering, materials science, and biology.

X-ray photoelectron spectroscopy (XPS)

X-ray photoelectron spectroscopy (XPS) is one of the surface analysis methods using X-rays, and it is possible to know the atomic types, electron states of each element, and relative amounts of each element. When the sample is irradiated with X-rays, photoelectrons are emitted from the inner shell of an atom by a photoelectric effect. If the

energy of an incident X-ray is defined as hν and the kinetic energy of a photoelectron is defined as Ekin, the binding energy Eb of an inner shell electron is expressed by the following formula.

$$E_b = h\nu - E_{kin} \quad \text{(Equation 2-3)}$$

In XPS, the kinetic energy E_{kin} of photoelectrons is measured to calculate the binding energy E_b of inner shell electrons. Because the distribution of binding energy E_b depends on the valence of the element, it is possible to identify atomic species present on the surface by examining peak positions in the XPS spectrum. In addition, since the binding energy varies with changes in the electron state of an atom, the electron state of a specific element can be known by peak fitting analysis of the XPS spectrum. Further, the relative amount of each element present in the sample can be found by examining the area of the peak. X-ray irradiation not only excites the surface but also electrons of atoms in the bulk, but most of them are scattered in the bulk lose kinetic energy, and remain inside the sample. Consequently, most of the photoelectrons detected by XPS are emitted from the vicinity of the surface. From this, it can be said that XPS is surface-sensitive and suitable for surface element analysis.

During XPS measurement, a charge-up phenomenon occurs in which electric charges accumulate on the sample surface. The energy correction is necessary because the charge-up shifts the energy of the peak in the measured XPS spectrum. Normally, energy correction is performed based on the C1s peak (284.2 eV), but in this study, *o*-AA

as an organic compound, is modified to the TiO_2(110) surface, so different energy peaks are mixed around the C1s peak. Therefore, it is inappropriate to use the C1s peak for energy correction in this experiment. Therefore, in this experiment, energy correction was performed based on the $Ti2p_{3/2}$ peak (458.7 eV).

In addition, the photoelectrons generated in XPS lose kinetic energy due to scattering and are detected at energies smaller than actual kinetic energy. As a result, a signal by electrons that have lost kinetic energy appears at a position different from the peak. This signal is called a background, and the background must be removed when calculating peak intensity or analyzing peak fitting. In this study, the background of all XPS spectra was removed by the Shirley method.

X-ray absorption fine structure (XAFS)

When X-rays are applied to a sample, X-rays are absorbed internally, and attenuated transmitted light comes out of the sample. By measuring incident and transmitted light, the absorption coefficient of a sample through which X-rays pass is obtained. An X-ray absorption spectrum is obtained by changing the energy (wavelength) of an X-ray and plotting the absorption coefficient against the energy of an X-ray. Observation of the X-ray absorption spectrum, it can be seen that there is an edge where the absorption coefficient increases rapidly at a specific energy, as shown in Figure 2-7.[17] This edge is called the absorption end, and the X-ray absorption coefficient increases

rapidly because the X-ray energy matches the ionization energy of the atom that absorbs X-rays to produce photoelectrons. The emitted photoelectrons are scattered internally and interfere with X-rays, and the intensity of X-rays after sample transmission varies due to interference. As a result, a vibration structure is seen in the range of 50-1000 eV from the absorption end of the X-ray absorption spectrum-ray absorption fine structure, abbreviated as XAFS. XAFS is divided into X-ray absorption near edge structure (XANES) and extended X-ray absorption fine structure (EXAFS). Because the causes of micro-vibration structures of X-ray absorption spectra are different in these two regions, structural information obtained by analysis is also different between XANES and EXAFS. These characteristics are described below.

X-ray absorption near edge structure (XANES)

XANES is the spectrum of an energy region from the absorption end to 50 eV in the XAFS spectrum. In the XANES region, the electrons that absorbed X-rays have not yet escaped from the atom and are transitioning to a quasi-continuous state. Therefore, the spectrum in the XANES region strongly reflects the electron state of the absorption atom. By analyzing the peak position and height of the spectrum in the XANES region, electron states, bond orientations, and symmetry of absorption atoms can be clarified.

Extended X-ray absorption fine structure (EXAFS)

EXAFS is a spectrum in the energy region from 50 eV to about 1000 eV of the XAFS spectrum. In the EXAFS region, unlike in the XANES region, photoelectrons that absorb X-rays protrude outside the atom. The protruding photoelectrons are scattered in atoms around the absorption atom and interfere with X-rays, resulting in a vibrational structure in the X-ray absorption spectrum. Since this phenomenon occurs in the EXAFS region, the spectrum strongly reflects the structure around the absorption atom.

EXAFS oscillations obtained by subtracting the background from the measured X-ray absorption spectrum have the property of increasing coordination numbers around absorption atoms (reducing coordination numbers) and decreasing coupling distances. In addition, when heavy elements such as metals are coordinated around the absorption atom, attenuation of EXAFS vibration is reduced, and conversely, attenuation of vibration is increased when light elements are coordinated around it. Analyzing EXAFS vibrations extracted from X-ray absorption spectra is a remarkably effective method for clarifying the local structure of the sample because atomic types, coordination numbers, and bond distances of each element are known.

Conventional XAFS uses a method called transmission, which irradiates powder samples with X-rays and measures the X-rays before irradiation and after the sample is transmitted. The principle of transmission method XAFS is explained below. An absorption coefficient μ(E) of X-ray energy E is expressed as follows by X-ray intensity

I_0(E) before transmission and X-ray intensity I(E) after transmission.

$$\frac{I(E)}{I_0(E)} = exp\,[-\mu(E)] \quad \text{(Equation 2-4)}$$

EXAFS vibration χ(k) is expressed as follows.

$$\chi(\mathrm{k}) = \frac{\mu(k)-\mu_0(k)}{\mu_0(k)} \quad \text{(Equation 2-5)}$$

μ(k) is obtained by converting the absorption coefficient μ(E) into a function of the number k of X-rays. μ_0(k) is the background coefficient, which is the absorption coefficient if the absorption atoms are assumed to be isolated. Because it is difficult to obtain the background experimentally, XAFS analysis software uses fitting functions such as Victoria expression to extrapolate the background and subtract it from the measured spectrum.

Further, the relation between energy E of X-ray and wave number k is shown as follows.

$$\mathrm{k} = \sqrt{2m(E-E_0)\hbar^2} \quad \text{(Equation 2-6)}$$

Here, E_0 is X-ray energy at the absorption end, m is the mass of electrons, and $\hbar$ is a Dirac constant (= h / 2π, h is a Planck constant).

The EXAFS oscillation χ_i(k) due to the ith bond with the absorption atom is expressed by the following formula.

$$\chi_i(\mathrm{k}) = \mathrm{A}_i(k)\sin(2kR_i + \delta_i(k)) \quad \text{(Equation 2-7)}$$

$$\mathrm{A}_i(k) = \left[\frac{S_0^2(k)}{kR_i^2}\right]|f_i(k,\pi)|exp(-2\sigma_i^2k^2)exp\left(-\frac{2R_i}{\lambda}\right) \quad \text{(Equation 2-8)}$$

$S_0^2(k)$: Intrinsic loss factor

$f_i(k,\pi)$: Backscattering amplitude

$\delta_i(k)$: Phase shift

λ : Mean free path

R_i : Bond distance

σ_i : Thermal vibration (Debye Waller factor)

Because the backscattering factor $f_i(k,\pi)$ and phase shift depend on the atomic species of the absorption and scattering atoms, these two functions are determined by determining atomic species. A Debye-Waller factor represents a contribution to the attenuation of EXAFS vibration caused by static disturbance, thermal vibration, and so on. An amplitude attenuation term $S_0^2(k)$ usually takes a value between 0.8 and 1. The EXAFS oscillation $\chi(k)$ measured in the experiment is the sum of EXAFS oscillations $\chi_i(k)$ due to the bonds of each atom around the absorption atom,

$$\chi(k) = \sum \chi_i(k) \quad \text{(Equation 2-9)}$$

Here, a spherical surface with the coupling distance R_i as a radius is considered, and this spherical surface is defined as an ith shell (shell). If N atoms are coordinated in the ith shell, the EXAFS oscillation $\chi_j(k)$ by each shell is expressed by the following formula.

$$\chi_j(k) = \sum \chi_i(k) = N\chi_i(k) \quad \text{(Equation 2-10)}$$

combining the above expressions, $\chi_j(k)$ is expressed as follows.

$$\chi_j(\mathrm{k}) = N\left[\frac{S_0^2(k)}{kR_i^2}\right]|f_i(k,\pi)|exp(-2\sigma_i^2k^2)exp\left(-\frac{2R_i}{\lambda}\right)\sin(2kR_i+\delta_i(k))$$

(Equation 2-11)

Thus, EXAFS vibration is the sum of attenuated sine waves. For this reason, in EXAFS analysis software, a method for extracting components of vibration using Fourier transform is used.

Data analysis of EXAFS by Curve fitting method

EXAFS is usually analyzed using the non-linear least square fitting method. This method is often called as curve fitting method. The equation is used to fit the observed data so that parameters are coordination numbers(*N*), correction of the origin of kinetic energy zero(ΔE_0), bond lengths(*r*), and Debye-Waller factors(σ^2). The backscattering amplitude and phase shift were calculated by FEFF code. The residual of EXAFS oscillation between the experimental data and the calculated one is minimized in the curve fitting method. The degree of fitting is evaluated by the *R*-factor as shown in Equation.

$$R-\mathrm{factor} = \frac{\sum_i\{k^n\cdot\chi_{data,i}(k)-k^n\cdot\chi_{calculated,i}(k)\}^2}{\sum_i\{k^n\cdot\chi_{data,i}(k)\}^2}$$ (Equation 2-12)

Here, χ_{data} and $\chi_{calculated}$ were EXAFS oscillation of experimental data and calculated one, respectively, k^n was weighted value and *n*=0, 1, 2, or 3. The region of *R*-factor calculation was the *k*-range which used for Fourier transformation. These definitions were the same as the REX2000 program (RIGAKU).

The degree of freedom, M, for fitting parameters is determined by Nyquist's theory.

$$M = \frac{2\Delta k \Delta r}{\pi} + \alpha \quad (\alpha = 0,1,2) \text{ (Equation 2-13)}$$

Here, Δk and Δr are the regions when the observed data is Fourier and inversely Fourier transformed. When the curve fitting analysis is carried out in r space, Δr is the range of curve fitting analysis. The degree of freedom is a fundamental limitation to the amount of information that how many parameters can be determined by an EXAFS spectrum. Therefore, the number of search parameters on curve fitting analysis must not exceed this degree of freedom to obtain reliable results. From Equation 2-13, it is expected that the way to increase the degree of freedom is to measure as large a k range as possible at EXAFS measurement. The EXAFS oscillation damps at high k region because 1: the scattering ability of the surrounding atom for the electron with high k wave numbers (or large momenta) becomes small, 2: the reduction factors of $1/k$ term in, and 3: Debye-Waller factor due to the thermal and static disorder. The thermal disorder can be reduced by the low-temperature measurement. The EXAFS measurement at low temperatures is recommended to obtain the high k-region data with good quality. In this thesis, all procedures are performed with the use of the computer software package named REX2000 and FEFF. The curve fitting analysis was performed in k-space in the range of 3.5 to 9 $Å^{-1}$ and in the r-range of 0.98 to 1.96 Å.

Polarization-dependent total reflection fluorescence XAFS (PTRF-XAFS)

In a normal transmission method XAFS using a powder sample as described above, information obtained by averaging structural information in three directions of the sample is obtained as a result of spectral analysis. This is due to the isotropic nature of the powder sample. As the structural information of the anisotropic sample varies depending on the azimuth to be measured, it is difficult to elucidate the three-dimensional structure of the anisotropic sample by a normal transmission method XAFS in which structural information of three azimuths is averaged. Because TiO_2(110) single crystal surfaces used in this study are also anisotropic, it is difficult to determine the three-dimensional structure of the surface by transmission method XAFS.

By using polarization characteristics of the XAFS, structural information of respective unaveraged three directions can be extracted. Because X-rays are electromagnetic waves, electric and magnetic fields vibrate perpendicular to each other. The angle to the combination of spectral intensity and electric field vector is related as shown in Figure 2-8, and the coordination value varies with the angle. Consequently, by moving the single crystal substrate relative to the electric field vector and changing the direction, information in three directions concerning coupling on the single crystal can be obtained. XAFS spectrum of s-pol (E//[$1\bar{1}0$]) and is-pol (E//[001]) can be measured by making a substrate horizontal to an electric field vector, and p-pol (E/[110]) can be measured by standing the substrate vertically (Figure 2-9) because EXAFS oscillation

$\chi(k)$ at K and L edges have the polarization dependence.

For K and L_1 absorption edges,

$$\chi_{obs}(k) = \sum_i 3\cos^2\theta_i \cdot \chi_i(k) \quad \text{(Equation 2-14)}$$

For L_2 and L_3 absorption edges,

$$\chi_{obs}(k) = \sum_i (0.7 + 0.9\cos^2\theta_i) \cdot \chi_i(k) \quad \text{(Equation 2-15)}$$

where θ_i is an angle between the polarization vector of $\vec{E}$ of the incident X-ray and the bond vector. Here, θ_i is a bond angle between the i_{th} atom and the absorption atom, and N is an effective coordination number. A coordination number obtained by the transmission method EXAFS is obtained by averaging coordination numbers in three directions, but in the case of polarization EXAFS, the coordination number appearing as structural information varies according to an X-ray electric field vector and coupling angle. Consequently, the angle of coupling can be estimated by comparing the effective coordination numbers of EXAFS oscillations in three directions. Polarization characteristics can also be seen in XANES. By comparing the heights of the peaks of XANES in three directions, it is possible to elucidate the orientation of π bonds and bonds between absorption atoms and adjacent atoms, symmetry of bonds, and so on.

Ultra-High-Vacuum (UHV) environment

To study the properties of a surface with well-defined atomic characteristics, the

surface composition must remain essentially constant throughout an experiment. This requirement implies that the influx of reactive species from the surrounding gas phase must be kept at a low rate. A reasonable criterion for this would be that only a small fraction, perhaps no more than a few percent, of an atomic layer of atoms should adhere to the surface from the gas phase within the experimental time.

UHV systems maintain extremely low pressures, minimizing the presence of gas molecules and contaminants in the experimental chamber. This is essential for studying surfaces at the atomic level because even small amounts of contaminated molecules can significantly impact the accuracy and reliability of measurements. In addition, UHV conditions help prevent interactions with molecules from the surrounding environment, preserving the integrity of the surface and allowing to observation precise surface during measurement. In other words, In UHV, surfaces are less prone to oxidation and other chemical reactions that might alter their properties. This stability is crucial for studying long-term effects and dynamic processes occurring on surfaces over extended periods.

Many surface science techniques, such as photoelectron spectroscopy and scanning tunneling microscopy, rely on the interaction of electrons with the surface. In UHV, the mean free path of electrons is increased, meaning that electrons can travel longer distances without colliding with gas molecules. This enhances the accuracy and depth resolution of surface analyses. The mean free path is the distance that a particle, take nitrogen molecules as an example in this case, travels on average between collisions.

$$\lambda = \frac{\bar{v}}{Z} = \frac{k_B T}{\sqrt{2}\sigma p} \quad \text{(Equation 2-16)}$$

$\bar{v}$: the mean velocity of the nitrogen molecules in an ideal gas in $m \cdot s^{-1}$

Z : the collision frequency in s^{-1}

k_B : the Boltzmann constant with the dimension of $m^2 \cdot kg \cdot s^{-2} \cdot K^{-1}$

T : temperature (K)

σ : collision cross-section of the nitrogen molecules in m^2 (0.42 nm^2 in N_2)

p : gas pressure in Pa

According to the equation, the mean free path of the nitrogen molecules in the atmospheric pressure (101.3 kPa) is just 70 nm, whereas at around 1×10^{-8} Pa environment the mean free path could be longer than 500 km. Therefore, the electron-based surface science approaches are usually conducted under UHV conditions where the pressure is lower than 10^{-5} Pa, such that the mean free path is longer than a hundred meters.

UHV condition also provides researchers with a controlled environment where they can precisely manipulate and monitor surface reactions. The absence of gases and contaminants allows for more reproducible and controlled experiments, enabling a deeper understanding of surface properties and reactions. Therefore, UHV systems are indispensable in surface science because they provide the necessary conditions for precise, uncontaminated, and controlled investigations of surfaces at the atomic level, facilitating a deeper understanding of surface properties and reactions.

Operando PTRF-XAFS measurement

As it was introduced above, the PTRF-XAFS measurements required high flux and energy X-rays that can only be generated by synchrotron radiation facilities. It means we must prepare the samples in the facility. Another UHV system was therefore settled in the Photon Factory at the Institute of Materials Structure Science (KEK-IMSS-PF, Tsukuba, Japan).

Density functional theory (DFT)

In this thesis, Density Functional Theory (DFT) was applied to modify the structure of the resulting material, because the DFT calculation shows better accuracy and lower computational cost. It provides a generalized quantum mechanical treatment of inhomogeneous electronic systems, whereby complete descriptions of the electronic structure of these systems can be determined solely by their electron density. There are many factors and basic sets for the calculation, here I describe when I used the conditions for this study.

All methods can be implemented through the VASP program.[18, 19] The Vienna ab initio simulation package (VASP) is a computer program for atomic scale materials modeling, for example, electronic-structure calculations and quantum-mechanical molecular dynamics, from first principles. VASP computes an approximate solution to the

many-body Schrödinger equation, either within density-functional theory (DFT), solving the Kohn-Sham (KS) equations, or within the Hartree-Fock (HF) approximation, solving the Roothaan equations. In VASP, central quantities, like the one-electron orbitals and electronic charge density, and the local potential are expressed in plane-wave basis sets. The electronic interactions are described using pseudopotentials and the projector-augmented-wave method (PAWs). This VASP software's ability to perform these tasks makes it an ideal program to perform DFT calculations of electronic structures of the adsorption of various potential molecules on crystalline substrates, to study theoretical understanding.

DFT calculations were performed under periodic boundary conditions using the Vienna Ab initio Simulation Package (VASP) version 5.4.1.[18, 19] The projector augmented wave (PAW) method[20-22] was adopted for calculations with spin polarization and van der Waals corrections (DFT-D3).[23] Iterative electronic relaxations are done such that energy differences (E_{diff}) between two successive steps should not exceed 10^{-5} eV. The Perdew−Burke−Ernzerhof (PBE) exchange-correlation functional was used for calculations within the generalized gradient approximation (GGA) applied for the exchange-correlation interaction.[24] A Brillouin zone was sampled using 1×1×1 Γ-centered k-point grids for optimization and 5×5×3 Monkhorst-Pack grids for density of state (DOS) calculation, respectively. The strong onsite Coulombic interactions of the Ti2p states were corrected using the Hubbard U term method (DFT+U), and 5.0 eV was used

for $U_{effective}$ (= U − J).[25] A crystal structure of bulk TiO_2 was obtained from the Materials Project database.[26] The calculated lattice constant was a=4.59 Å and c=3.00 Å, which is consistent with the computational value of a=4.59 Å and c=2.96 Å and the experimental value of a=4.58 Å and c=2.94 Å.[27] The molecular models were visualized using Chemcraft software.

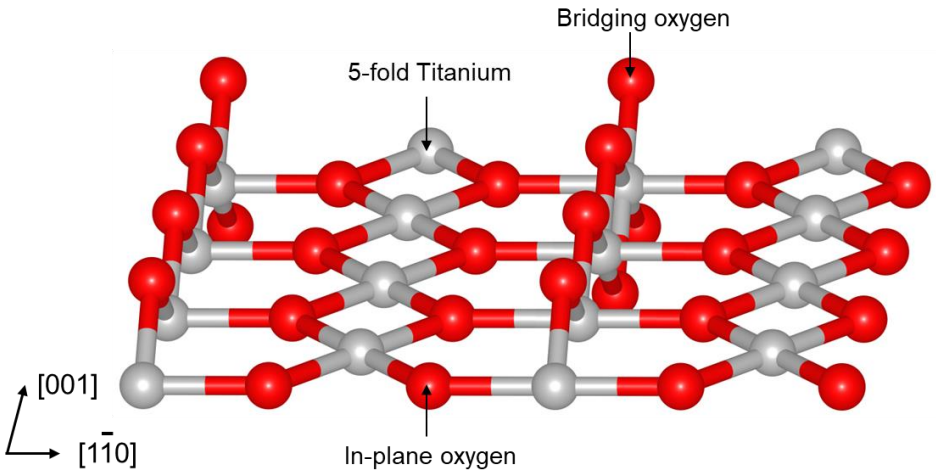

Figure 2-1. TiO_2(110) surface.

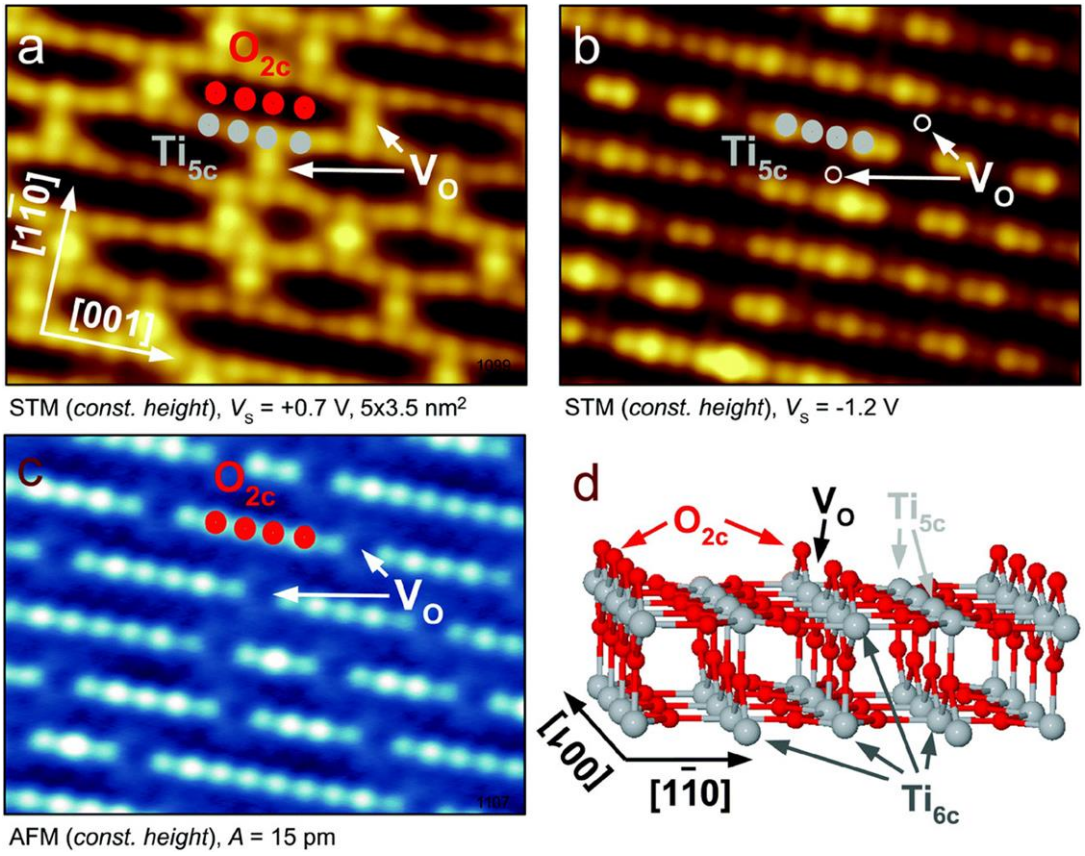

Figure 2-2. STM and nc-AFM imaging of the rutile TiO_2 (110) surface. The same area of the sample is shown with (a) empty states STM, (b) filled states STM, and (c) AFM. All images were measured at a sample temperature T = 78 K. (d) Structural model of the surface. STM and AFM images were measured in constant-height mode and adapted from ref 7.

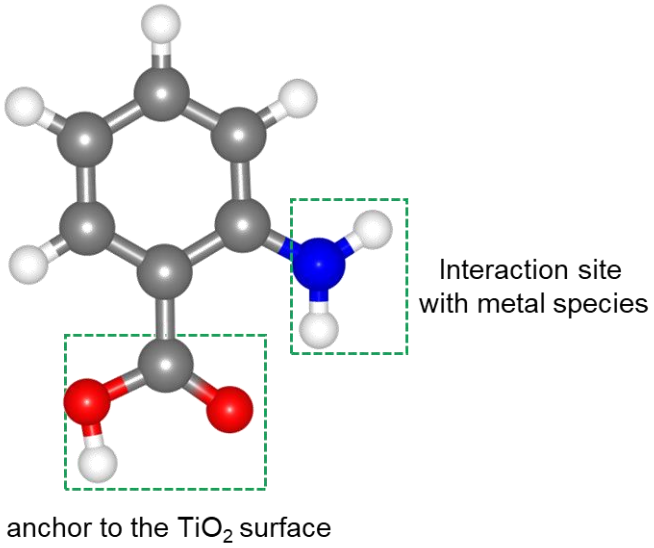

Figure 2-3. *o*-anthranilic acid. The white, dark gray, red, and blue colors indicate H, C, O, and N atoms, respectively.

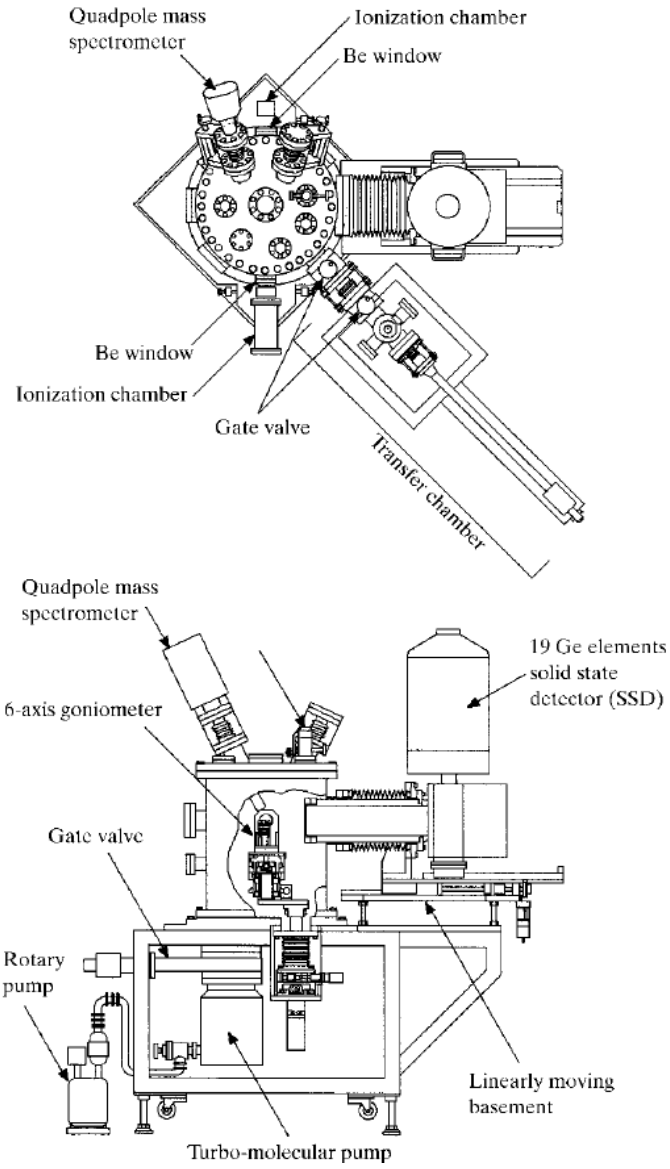

Figure 2-4. The *in-situ* polarization-dependent total-reflection fluorescence (PTRF)-XAFS measurement chamber with the sample-transfer chamber. Adapted from ref 9.

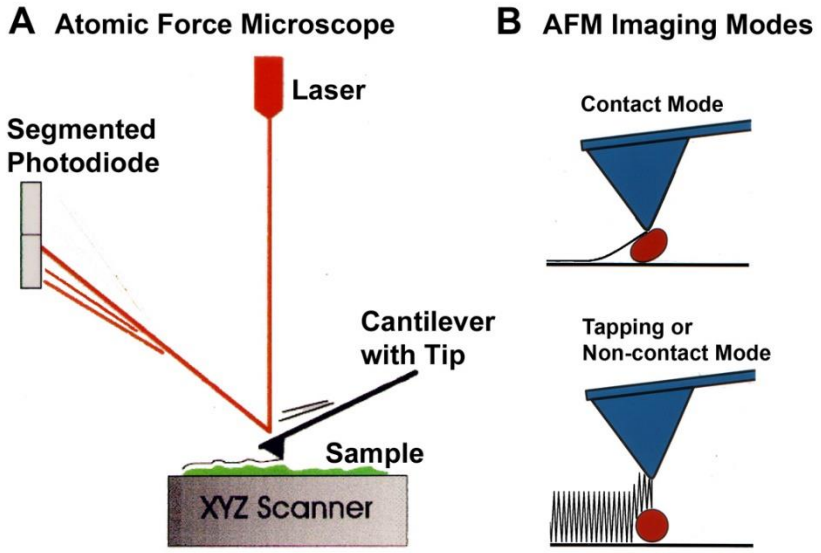

Figure 2-5. The schematic image of the atomic force microscope.

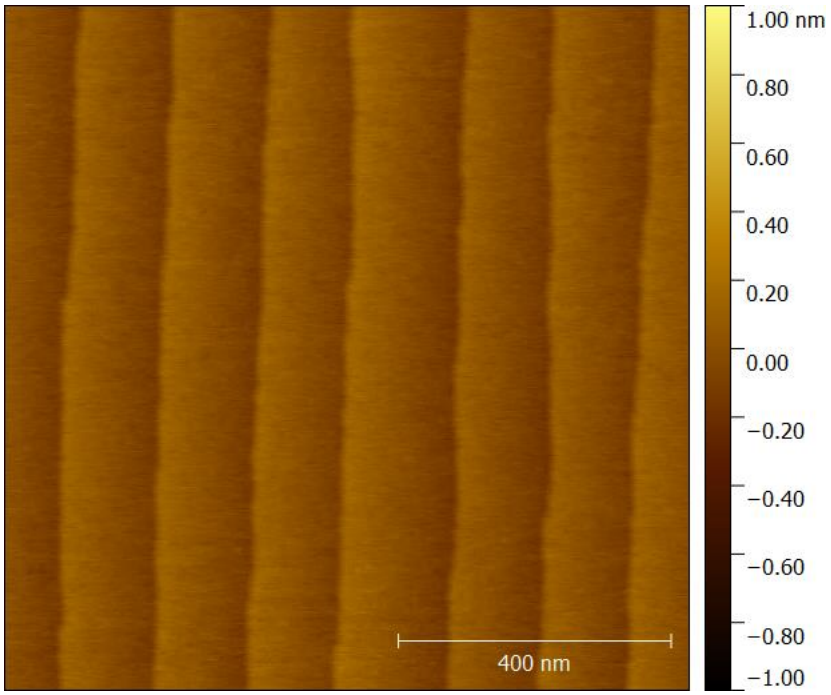

Figure 2-6. Atomic force microscope image of TiO_2(110) surface. Observed data was applied by the Gwyddion graphical software.

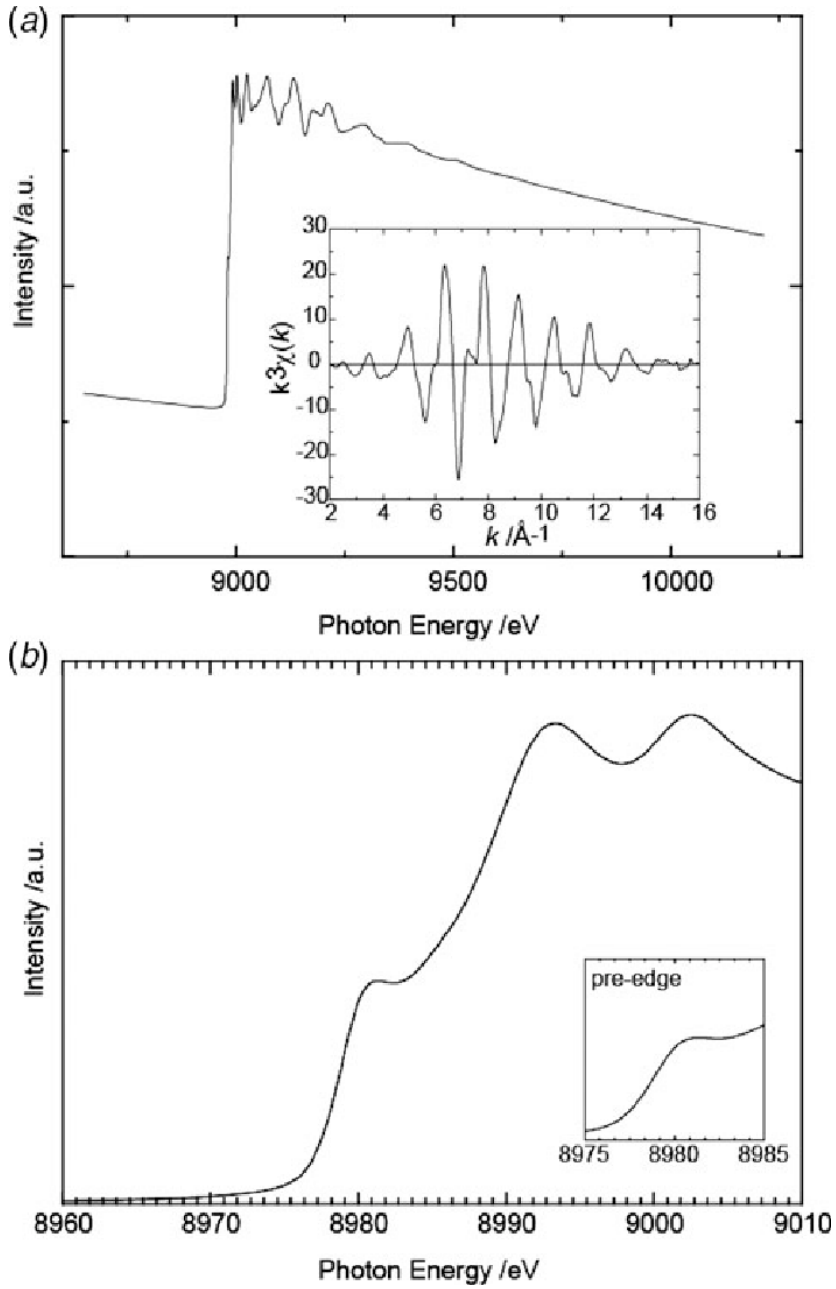

Figure 2-7. Cu K-edge XAFs for Cu foil. Adapted ref 17.

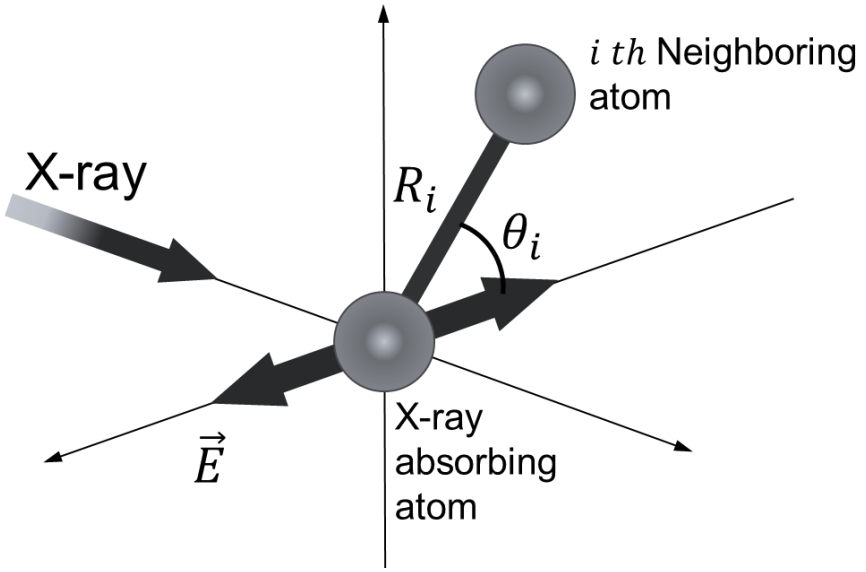

Figure 2-8. Polarization dependence of XAFS oscillation $\chi(k)$.

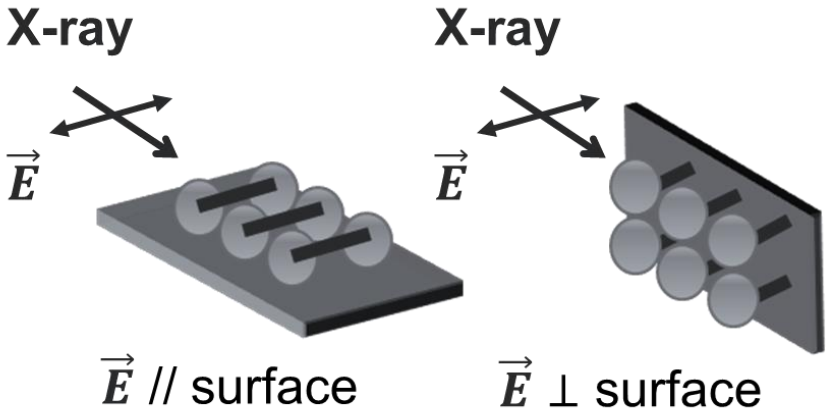

Figure 2-9. Determination of sample direction by PTRF-XAFS measurements.

Reference

1 U. Diebold, *Surface Science Reports* **2003**, *48*, 53.

2 Z. Dohnálek, I. Lyubinetsky, R. Rousseau, *Progress in Surface Science* **2010**, *85*, 161.

3 H. Onishi, Y. Iwasawa, *Surface Science* **1994**, *313*, L783.

4 R. Lindsay, A. Wander, A. Ernst, B. Montanari, G. Thornton, N. Harrison, *Physical review letters* **2005**, *94*, 246102.

5 G. Cabailh, X. Torrelles, R. Lindsay, O. Bikondoa, I. Joumard, J. Zegenhagen, G. Thornton, *Physical Review B* **2007**, *75*, 241403.

6 W. Busayaporn, X. Torrelles, A. Wander, S. Tomić, A. Ernst, B. Montanari, N. Harrison, O. Bikondoa, I. Joumard, J. Zegenhagen, *Physical Review B* **2010**, *81*, 153404.

7 M. Reticcioli, M. Setvin, X. Hao, P. Flauger, G. Kresse, M. Schmid, U. Diebold, C. Franchini, *Physical Review X* **2017**, *7*, 031053.

8 C. Lun Pang, R. Lindsay, G. Thornton, *Chemical Society Reviews* **2008**, *37*, 2328.

9 W.-J. Chun, Y. Tanizawa, T. Shido, Y. Iwasawa, M. Nomura, K. Asakura, *Journal of Synchrotron Radiation* **2001**, *8*, 168.

10 J. C. Green, P. Decleva, *Coordination Chemistry Reviews* **2005**, *249*, 209.

11 G. G. Fuentes, E. Elizalde, F. Yubero, J. M. Sanz, *Surface and Interface Analysis* **2002**, *33*, 230.

12 F. J. Giessibl, *Reviews of Modern Physics* **2003**, *75*, 949.

13 G. Binnig, C. F. Quate, C. Gerber, *Phys Rev Lett* **1986**, *56*, 930.

14 Y. Martin, C. C. Williams, H. K. Wickramasinghe, *Journal of Applied Physics* **1987**, *61*, 4723.

15 Q. Zhong, D. Inniss, K. Kjoller, V. B. Elings, *Surface Science Letters* **1993**, *290*, L688.

16 P. K. Hansma, J. P. Cleveland, M. Radmacher, D. A. Walters, P. E. Hillner, M. Bezanilla, M. Fritz, D. Vie, H. G. Hansma, C. B. Prater, J. Massie, L. Fukunaga, J. Gurley, V. Elings, *Applied Physics Letters* **1994**, *64*, 1738.

17 S. Yoshioka, T. Ishioka, H. Okabe, A. Harata, Y. Sejima, K. Hara, T. Okajima, *Diamond Light Source Proceedings* **2011**, *1*, e129.

18 G. Kresse, J. Hafner, *Physical Review B* **1993**, *47*, 558.

19 G. Kresse, J. Furthmüller, *Computational Materials Science* **1996**, *6*, 15.

20 G. Kresse, D. Joubert, *Physical Review B* **1999**, *59*, 1758.

21 O. Bengone, M. Alouani, P. Blöchl, J. Hugel, *Physical Review B* **2000**, *62*, 16392.

22 P. E. Blöchl, *Physical Review B* **1994**, *50*, 17953.

23 S. Grimme, J. Antony, S. Ehrlich, H. Krieg, *The Journal of Chemical Physics* **2010**, *132*, 154104.

24 J. P. Perdew, K. Burke, M. Ernzerhof, *Physical Review Letters* **1996**, *77*, 3865.

25 T. T. Thoa, H. Van Hung, N. T. M. Hue, *Vietnam Journal of Chemistry* **2022**, *60*,

183.

26 A. Jain, S. P. Ong, G. Hautier, W. Chen, W. D. Richards, S. Dacek, S. Cholia, D. Gunter, D. Skinner, G. Ceder, K. A. Persson, *APL Materials* **2013**, *1*, 011002.

27 T. T. Thoa, T. T. Nguyen, H. Van Hung, N. T. M. Hue, *Vietnam Journal of Chemistry* **2023**, *61*, 563.

Chapter 3

Structural determination of atomic Cu dispersion on TiO_2 (110) surface premodified by amine-containing carboxylic compound

Introduction

Single-atom catalysts (SACs), which consist of isolated single metal atoms dispersed on a powdery oxide support, have recently attracted much attention due to their high catalytic activity and cost-saving of precious metals.[1-3] The SACs are usually obtained by immobilizing metal species on an oxide surface through surface OH groups or linker molecules that strongly interact with both the metal species and the support. However, the metal atoms often aggregate to form particles, particularly at high temperatures, due to insufficient interaction between the metal atoms and the support surface, and the factors for controlling atomic dispersion are not well understood.

W. Chun *et al.,* have developed a premodified surface method to obtain an atomically dispersed metal species on an oxide surface and applied polarization-dependent total reflection fluorescence X-ray absorption fine structure (PTRF-XAFS) to evaluate the 3D structures of such metal species at the atomic level.[4-9] When a TiO_2(110) surface is

premodified with sulfur-containing compounds such as mercaptobenzoic acid (*o, m, p*-MBA) and thiophene carbonic acid (TCA) as a linker molecule, we can obtain atomic dispersion of Ni,[5] Cu,[6,9] and even Au.[8] Almost linear S–metal–O structures were formed where the metal atoms were sandwiched by the sulfur atom of the linker molecule and the surface lattice oxygen of the TiO_2(110). We have proposed a new index ($R_{S–M–O}$ index) to judge the preference for single-atom formation. $R_{S–M–O}$ was defined as (D^0_{298} (M–S) + D^0_{298} (M–O)) / D^0_{298} (M–M), where D^0_{298} (M–S), D^0_{298} (M–O) and D^0_{298} (M–M) are the bond dissociation energies at 298 K for metal–sulfur, metal–oxygen and metal–metal bonds, respectively.[5] The higher the $R_{S–M–O}$ value is, the more the S–metal–O structure is preferred over metal aggregation. However, we are not sure if the *R* index applies to other linker molecules containing nitrogen or phosphorus atoms that also act as binding sites for the metal atoms. In this study, I focus on a Cu dispersion on a TiO_2(110) surface premodified with a nitrogen-containing compound (*o*-anthranilic acid, *o*-AA). The estimated $R_{N–Cu–O}$ value is 2.6 (Table 3-1)[10] which is lower than $R_{S–Cu–O}$ (3.1), and thus atomic dispersion of Cu may be less preferable. The valence state and 3D structure of the Cu species formed on the TiO_2(110) surface premodified with *o*-AA molecules were examined by the PTRF-XAFS technique to evaluate the effect of the premodification on the dispersion and local structure of the Cu species.

Preparation of Cu/o-AA/TiO_2(110)

A Nb-doped (0.05 wt.%) TiO_2(110) substrate (20×20×1 mm^3, Shinkosya Co., Japan) was cleaned by immersion in 10% HF aqueous solution for 10 minutes, followed by annealing in air at 700 ℃ for 1 hour. The cleaned surface was immersed in a 2 mM ethanol solution of *o*-AA (Wako Chemicals, Japan) for 24 hours to modify the TiO_2(110) surface with an *o*-AA monolayer. The surface morphology of the *o*-AA/TiO_2(110) was imaged using AFM (Cypher, Oxford Instruments). The sample was then transferred to the ultrahigh vacuum (UHV) PTRF-XAFS chamber and Cu was evaporated onto the *o*-AA/TiO_2(110) surface at room temperature by resistive heating of a tungsten filament wrapped with a Cu wire (99.999% purity, Nilaco Co., Japan). The Cu coverage on the Cu/*o*-AA/TiO_2(110) surface was estimated to be 0.1 ML from the XPS spectra of $Cu2p_{3/2}$ to $Ti2p_{3/2}$ peak area ratio, where 1 ML was defined as $5.2\times10^{14}/cm^2$ regarding the TiO_2(110)-(1×1) unit cell.

Surface characterization of o-AA/TiO_2(110)

According to the AFM measurement of *o*-AA/TiO_2(110), the premodified TiO_2(110) surface by *o*-AA molecule showed a rough surface but it is a clean surface without any cracks or aggregates on the TiO_2(110) surface (Figure 3-1a and 3-1b). Also, from the depth profile (Figure 3-1c and 3-1d), the height of TiO_2(110) steps on the surface

did not show a significant change before and after the adsorption of *o*-AA molecules, indicating that the surface is covered with *o*-AA molecules.

Cu deposition on o-AA/TiO_2(110)

Figure 3-2 shows the *o*-AA/TiO_2(110) surface before and after Cu deposition. In Figure 3-2a, the binding energy for the N1s peak for the *o*-AA/TiO_2(110) surface was 399.5 eV, which can be assigned to the N atoms of the NH_2 group of the adsorbed *o*-AA molecules. The N coverage was estimated to be 0.4 ML from the N1s to $Ti2p_{3/2}$ peak area ratio. After Cu deposition, the N1s peak position was slightly shifted to higher binding energy, indicating interaction and bond formation between the deposited Cu atoms and the N atoms. The N1s spectrum for the Cu/*o*-AA/TiO_2(110) was deconvoluted and well-fitted with two Gaussian peaks centered at binding energies of 399.5 and 400.5 eV, which can be assigned to N atoms interacting without and with Cu atoms. The N coverages with and without interaction with the Cu atoms were 0.1 and 0.3 ML, respectively. It is noted that the Cu coverage estimated from the $Cu2p_{3/2}$ to $Ti2p_{3/2}$ peak area ratio was also 0.1 ML, indicating that almost all the deposited Cu atoms reacted with the N atoms on the *o*-AA/TiO_2(110) surface. In the Cu2p XPS spectrum for the Cu/*o*-AA/TiO_2(110) (Figure 3-2b), the binding energy for the $Cu2p_{3/2}$ peak was 933.2 eV and no satellite peaks characteristic of Cu(II) were found in the 940~945 eV region, indicating that the Cu species were Cu(0) or Cu(I).

Structure determination of Cu/ o-AA/TiO_2(110)

Figures 3-3a and 3b show Cu K-edge PTRF-XANES spectra of the Cu/*o*-AA/TiO_2(110) and XANES spectra of Cu reference compounds, respectively. The XANES spectra of the Cu/*o*-AA/TiO_2(110) showed different features from that of Cu foil, indicating the formation of a non-metallic Cu species. The mid-edge features at around 8984 eV for all orientations could be assigned to the 1s−4pπ* dipole transition. The inflection points of the edge appeared at around 8981 eV for all orientations. The respective inflection points for Cu foil, Cu_2O, CuO, tetrakis(acetonitrile)copper(I) tetrafluoroborate ($Cu(MeCN)_4BF_4$) and copper(II) phthalocyanine (CuPc) were 8979.5, 8980.6, 8984.7, 8981.2, and 8985.1 eV, respectively. Considering the XANES and XPS results, the oxidation state of the Cu species on the *o*-AA/TiO_2(110) was assigned to be monovalent (Cu(I)). Figure 3-2(a) shows a significant polarization dependence, where a strong 1s−4pπ* peak is found for the [001] and $[1\bar{1}0]$ directions while the peak corresponding to 1s−4pσ* observed at around 8997 eV is stronger for the [110] direction, suggesting that the orientation of the Cu species is not random but ordered with respect to the TiO_2(110) surface.

Figure 3-4 shows Cu K-edge PTRF-EXAFS spectra of the Cu/*o*-AA/TiO_2(110), in addition to the EXAFS spectra of the Cu reference compounds. The envelopes of the PTRF-EXAFS oscillations are damped quickly in the higher *k* region, compared to that for Cu foil, indicating that the nearest neighbor atom of Cu is not Cu, but a lighter atom

such as nitrogen or oxygen. The polarization dependence is such that the amplitudes of the EXAFS oscillations in the [001] and [$1\bar{1}0$] directions are comparable but are smaller than that in the [110] direction. A curve fitting analysis indicated no contribution from Cu–Cu interaction, which suggests that no Cu aggregation occurred, while Cu–X (X=N, O) interaction is dominant in the three polarization directions (Table 3-2 and Figure 3-5). Previous results for direct Cu deposition on a TiO_2(110) surface revealed that Cu easily aggregated to form particles, even at an extremely low coverage of 0.03 ML. Therefore, Cu aggregation was effectively blocked on the surface by the presence of nitrogen atoms in coadsorbed *o*-AA molecules. The average distance of the Cu–X bonds and their coordination number were estimated to be 0.200±0.005 nm and ~2, respectively, as shown in Table 3-2. As suggested by the XPS results, one Cu atom interacted with one N atom to form a Cu–N bond. Therefore, considering that the coordination number was ~2, the oxygen atom of the TiO_2(110) was the other candidate to coordinate with the Cu atom.

To determine the accurate structure of the Cu species, an iteration method was employed using the FEFF code and real-space model structure. The model structure was constructed based on the following results and knowledge.

(1) Since typical Cu–N and Cu–O bond distances are 0.19~0.21 nm and 0.18~0.19 nm, respectively, the Cu–N distance should be longer than the Cu–O distance.

(2) The *o*-AA molecules were adsorbed on the TiO_2(110) surface with Ti(IV)–carboxylate bonding.

(3) We confirmed that the adsorbed *o*-AA molecules were not decomposed or desorbed after Cu deposition by the XPS measurements, suggesting that their molecular structure was preserved.

Figure 3-6 shows the proposed model structure that fulfills all the three conditions mentioned above. The calculated EXAFS oscillations using the proposed model were in good agreement with the observed spectra (Figure 3-7). The Cu–O bond distance was 0.193 nm, which was consistent with the Cu–O distance (0.196 nm) in Cu/acetic anhydride/TiO_2(110). The Cu–N bond distance in N–Cu–O bonding was 0.215 nm, which was slightly shorter than that for Cu–N (0.219 nm) in the Cu(CH_3CN). The Cu–N and Cu–O bonds were oriented 49° and 61° to the $[1\bar{1}0]$ direction, respectively, where the precision by FEFF simulation was less than 3°. The Cu–N and Cu–O bond angles to the surface normal (to the [110] direction) were 61° and 43°, respectively. The N–Cu–O bond angle was estimated to be 162°, which was similar to that for the linear O–Cu–O structure found in Cu/acetic anhydride/TiO_2(110). Since Many Cu(I) compounds had a linear structure accompanied by two ligands, it was concluded that Cu was monovalent. The formation of the almost linear N–Cu–O structure showed similarity to the S–Cu–O bonding in the Cu/*o*-MBA/TiO_2 (110). The N–Cu–O bond angle (162°) was slightly bent compared to the S–Cu–O angle (177°).

Conclusion

Atomically dispersed Cu atoms were formed on a TiO_2(110) surface by premodification with *o*-AA molecules, where the $R_{N–Cu–O}$ value is 2.6. The value is the lowest among those for single-metal dispersions on TiO_2(110) obtained by the premodified surface method (Table 3-1). According to the $R_{X–M–O}$ values in Table 3-1, the boundary value for a single-metal dispersion may be between 2.6 and 2. Thus, the $R_{X–M–O}$ index could roughly explain the trend of single-metal dispersion on a TiO_2(110) surface premodified with organic linker molecules. In addition, the selection of a different linker molecule for premodification of a TiO_2(110) surface offers a new strategy for fine-tuning the coordination environment around the atomically dispersed metal sites, which may lead to precise control of catalytic performance.

Table 3-1. Dissociation energies at 298 K (D^0_{298}) for metal−metal (M−M), metal−oxygen (M−O), metal−nitrogen (M−N) and metal−sulfur (M−S) bonds for Cu, Ni, Au, and Pt and the corresponding R_{N-M-O}, R_{S-M-O} and R_{O-M-O} values. R_{X-M-O}(X =N or S or O) is defined as (D^0_{298}(M−X) + D^0_{298}(M−O))/D^0_{298}(M−M). The symbols ○ and × indicate atomic dispersion and aggregation of the evaporated metal atoms, respectively, on the TiO_2(110) surface premodified with the corresponding organic molecules (o-anthranilic acid for R_{N-M-O}, o-mercaptobenzoic acid or thiophene carboxylic acid for R_{S-M-O}, and acetic anhydride for R_{O-M-O}).

Metal	D°_{298}(M−M) / kJ/mol	D°_{298}(M−O) / kJ/mol	D°_{298}(M−N) / kJ/mol	D°_{298}(M−S) / kJ/mol	R_{N-M-O}	R_{S-M-O}	R_{O-M-O}
Cu	177	269	192[a]	276	2.6 ○[b]	3.1 ○[5,9]	3.0 ○[7]
Ni	201	382	233[a]	344		3.6 ○[5]	
Au	226	221		418		2.8 ○[5]	2.0 ×[c]
Pt	307	246		233		1.6 ×[5]	

[a]D^0_{298}(M−N) values for Cu and Ni are quoted from dissociation energies for Cu^+−NH_2 and Ni^+−NH_2 bonds, respectively[10]. [b]Present work. [c]W.-J. Chun, Y. Koike, K. Ijima, H. Ashima, G. Tateno, M. Nomura, Y. Iwasawa, K. Asakura, PF activity report Part B **2006**, *24*, 63.

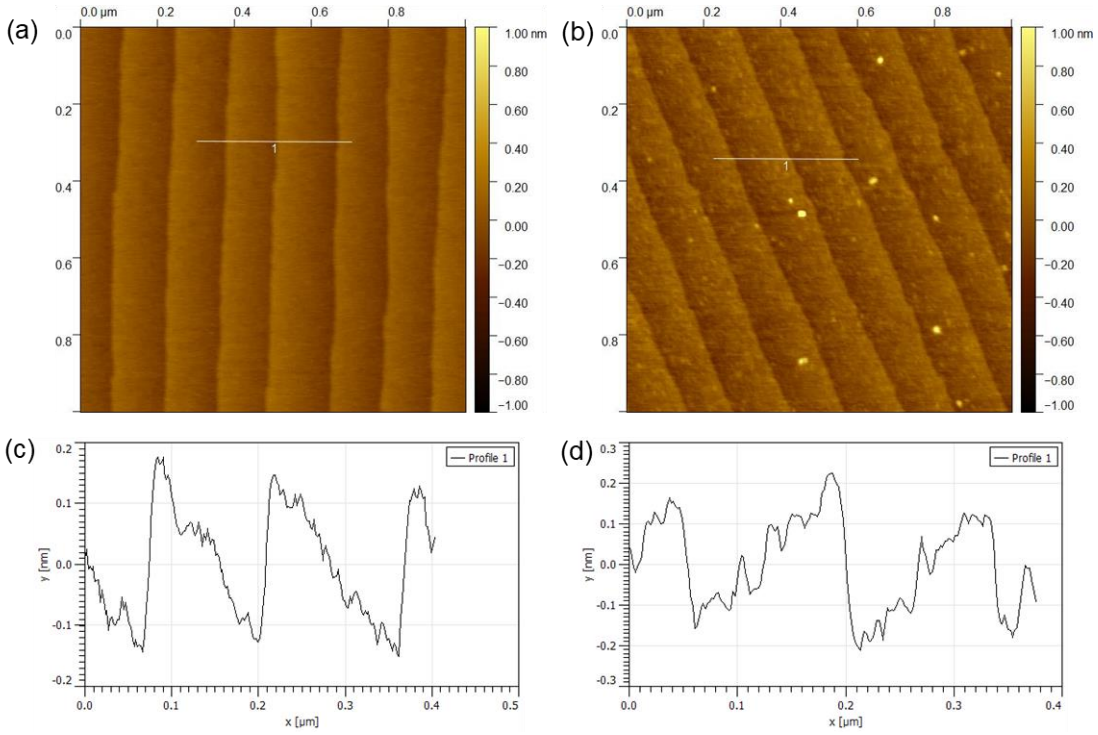

Figure 3-1. AFM images of (a) bare TiO_2(110) and (b) adsorption of *o*-AA on TiO_2(110). (c) and (d) show a depth profiling from AFM images of (a) and (b) respectively analyzed by computational software named Gwyddion.

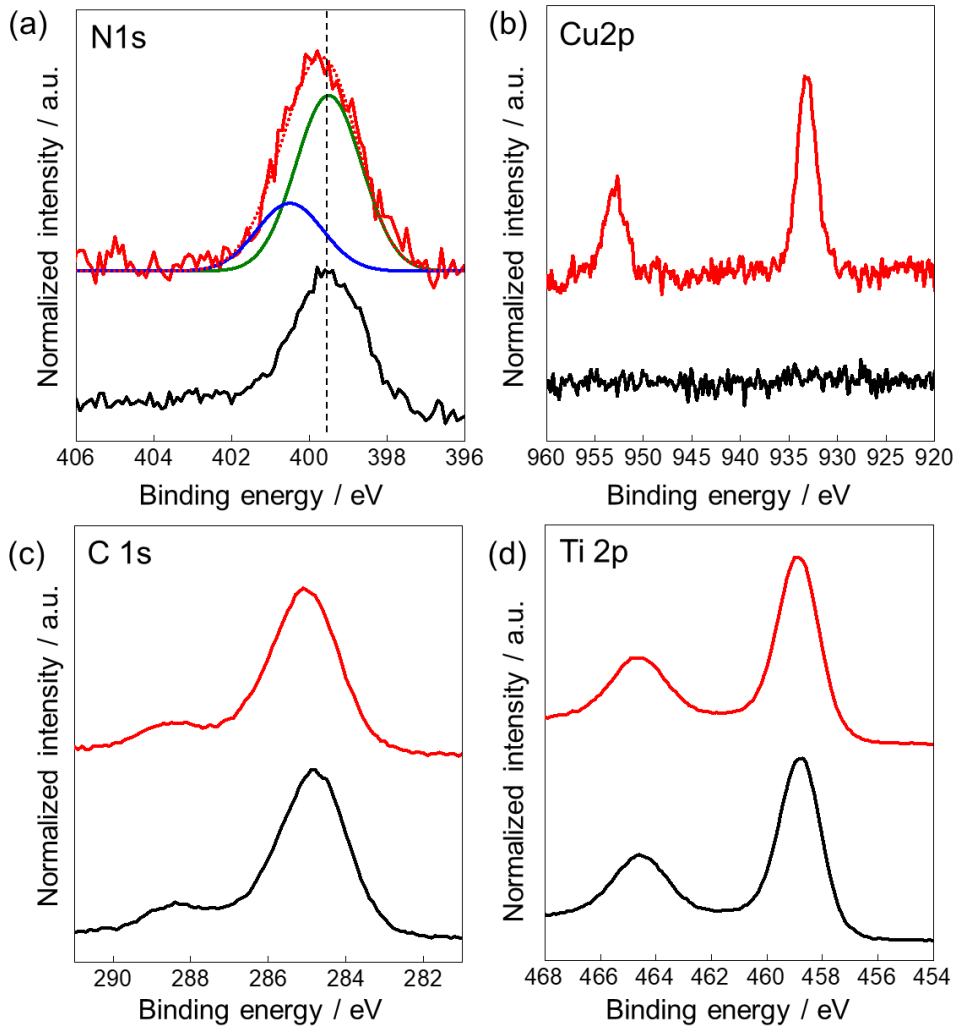

Figure 3-2. (a) N1s, (b) Cu2p, (c) C1s, and (d) Ti2p XPS spectra of *o*-AA/TiO_2(110) surface before (black solid line) and after Cu deposition (red solid line). In (a), deconvolution of the N1s peak was conducted using two Gaussian peaks (green and blue solid lines).

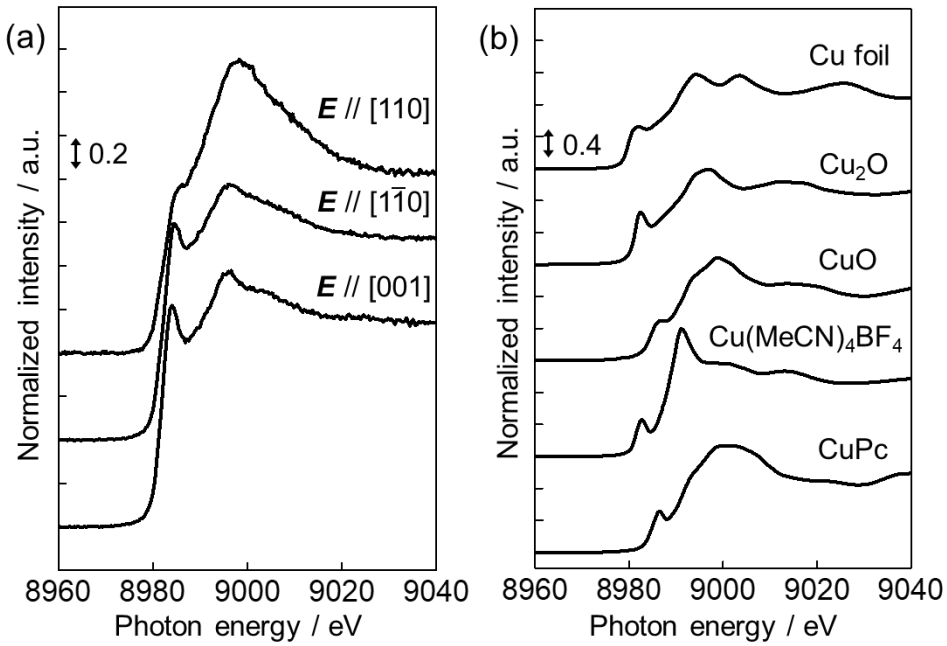

Figure 3-3. (a) Cu K-edge PTRF-XANES spectra of Cu/*o*-AA/TiO_2(110) were obtained in three different polarization directions. (b) Cu K-edge XANES spectra of reference compounds.

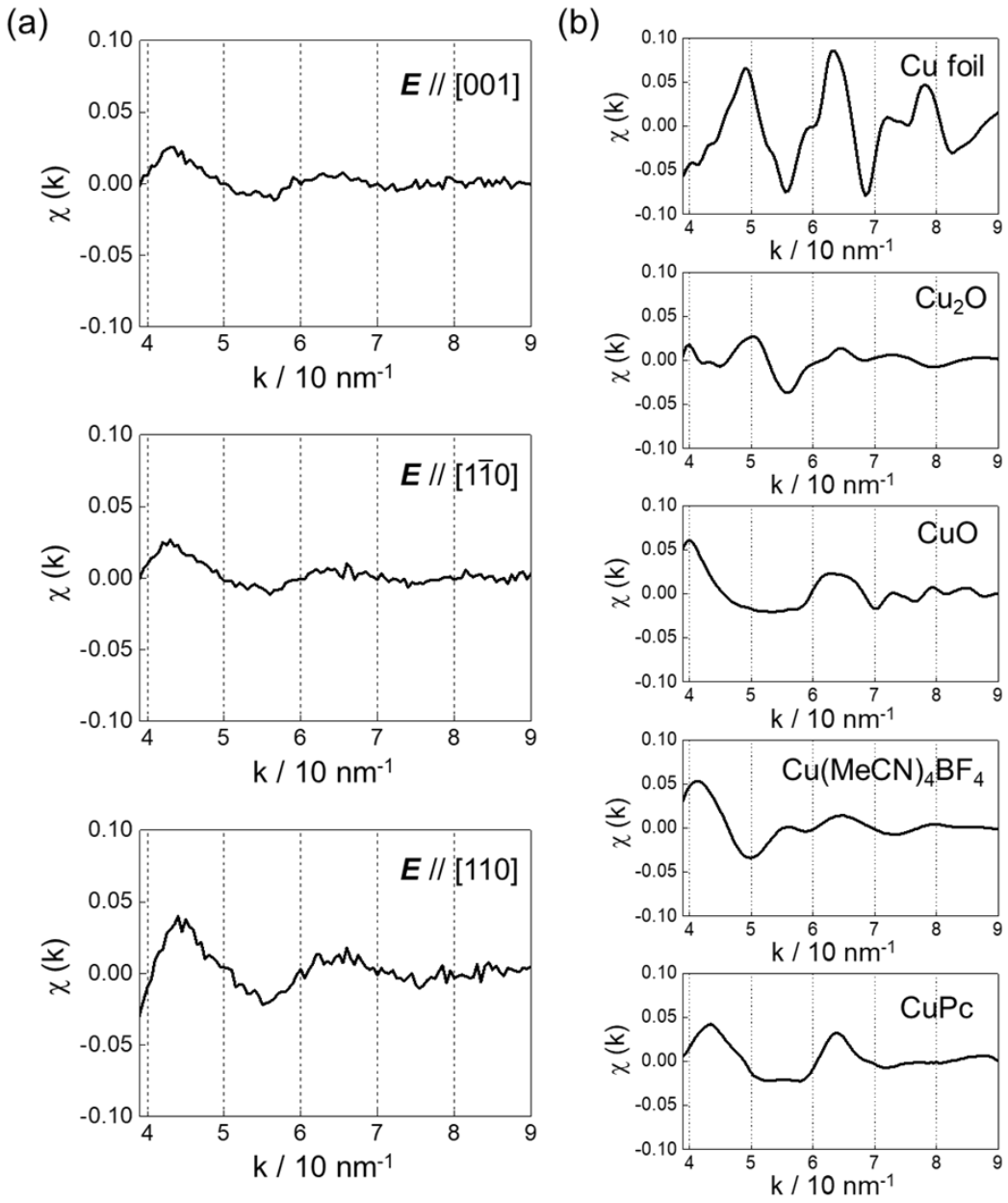

Figure 3-4. (a) Cu K-edge PTRF-EXAFS spectra of Cu/*o*-AA/TiO_2(110) were obtained in three different polarization directions. (b) Cu K-edge EXAFS spectra of reference compounds.

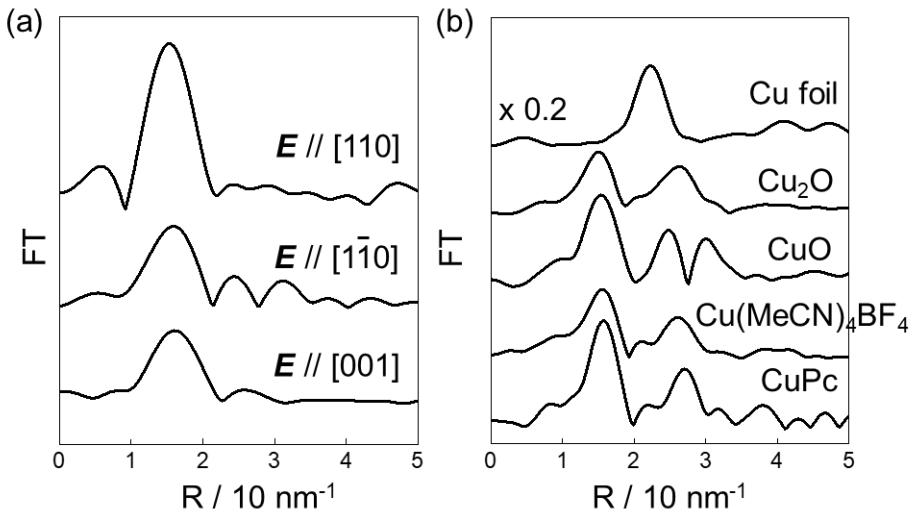

Figure 3-5. (a) Fourier transform (FT) of Cu K-edge $k^3\chi(k)$ PTRF-EXAFS spectra of Cu/*o*-AA/TiO_2(110) in three different polarization directions. (b) FT of Cu K-edge $k^3\chi(k)$ EXAFS spectra of Cu reference compounds.

Table 3-2. Curve fitting analysis for Cu K-edge PTRF-EXAFS spectra of Cu/*o*-AA/TiO_2(110) (Figure 3-5). Backscattering amplitude and phase shift values for nitrogen shell are obtained from the EXAFS measurement of tetrakis(acetonitrile)copper tetrafluoroborate ($Cu(MeCN)_4BF_4$) as reference material. The EXAFS fits were performed in k-space in the range of 3.5 to 9 $Å^{-1}$ and one shell (Cu−N) was used to fit the spectrum in the r-range of 0.98 to 1.96 Å.

	S. Atom	*N*	*r* / Å	*dE* / eV	*σ* / Å	*R*-factor / %
E // [001]	N	1.6±0.3	2.02±0.04	1.6±0.8	0.08±0.05	8.3
E // $[1\bar{1}0]$	N	1.8±0.4	2.00±0.04	1.6±0.6	0.09±0.04	8.8
E // [110]	N	2.9±0.5	1.98±0.04	1.6±0.6	0.07±0.05	8.7
average	N	2.2±0.3	2.00±0.05	1.6±0.6	0.08±0.05	8.4

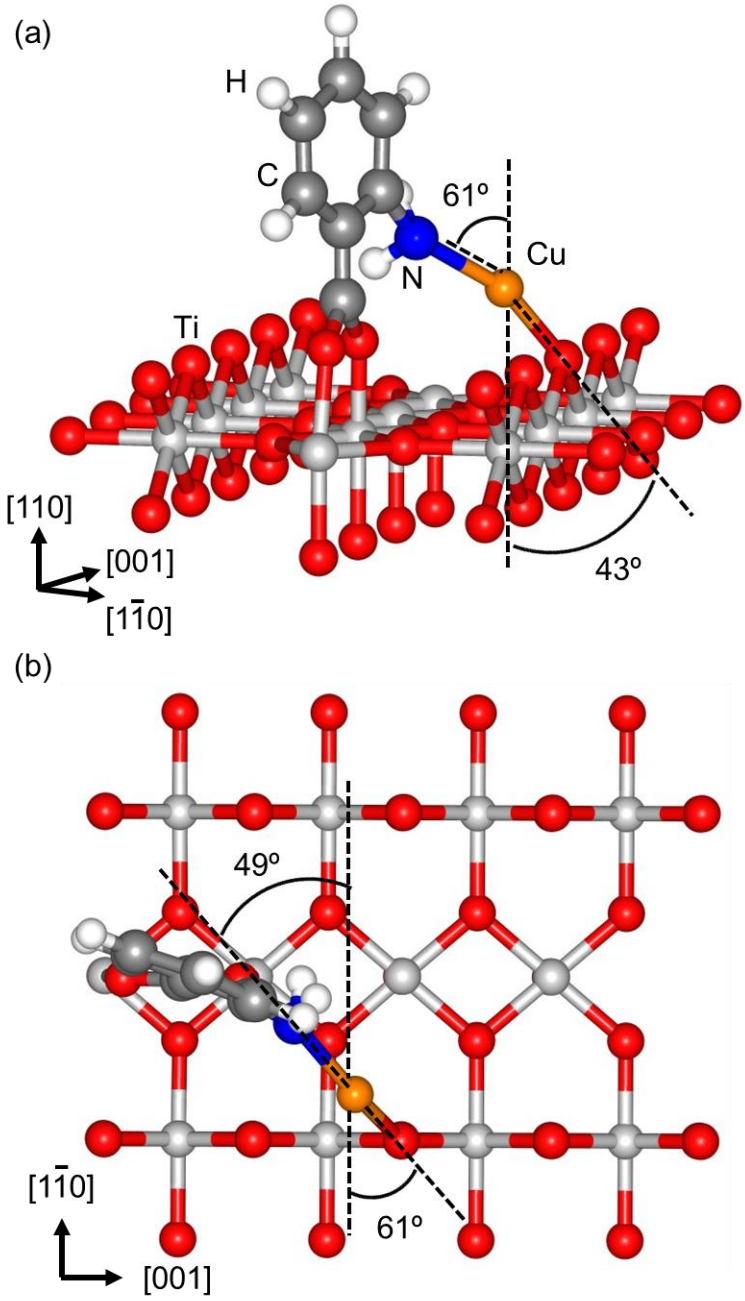

Figure 3-6. Proposed model structure for Cu/*o*-AA/TiO_2(110) surface. (a) side view and (b) top view.

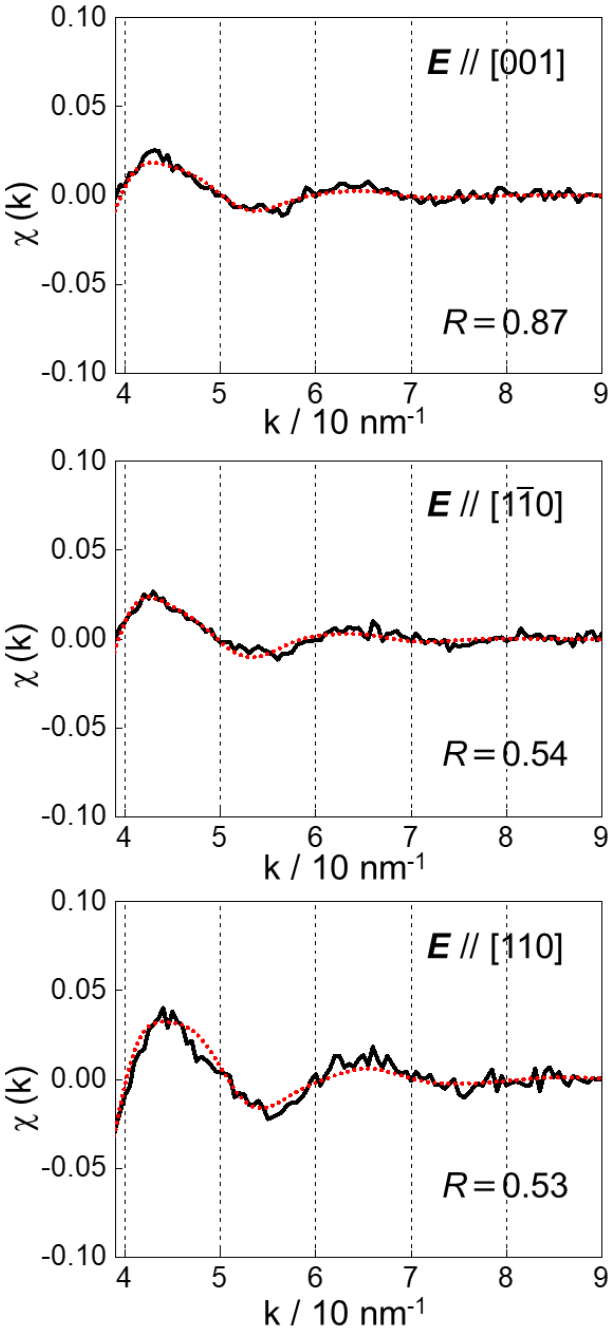

Figure 3-7. Comparison between observed PTRF-EXAFS spectra of Cu/*o*-AA/TiO_2(110) surface (black solid lines) and those calculated based on the model structure illustrated in Figure 3-6 (red dotted lines).

Reference

1 X.-F. Yang, A. Wang, B. Qiao, J. Li, J. Liu, T. Zhang, *Acc. Chem. Res*. **2013**, *46*, 1740.

2 L. Liu, A. Corma, *Chem. Rev.* **2018**, *118*, 4981.

3 S. K. Kaiser, Z. Chen, D. Faust Akl, S. Mitchell, J. Pérez-Ramírez, *Chem. Rev.* **2020**, *120*, 11703.

4 S. Takakusagi, Y. Iwasawa, K. Asakura, *Chem. Rec*. **2019**, *19*, 1244.

5 S. Takakusagi, A. Kunimoto, N. Sirisit, H. Uehara, T. Ohba, Y. Uemura, T. Wada, H. Ariga, W.-J. Chun, Y. Iwasawa, K. Asakura, *J. Phys. Chem. C* **2016**, *120*, 15785.

6 S. Takakusagi, H. Nojima, H. Ariga, H. Uehara, K. Miyazaki, W.-J. Chun, Y. Iwasawa, K. Asakura, *Phys. Chem. Chem. Phys*. **2013**, *15*, 14080.

7 W.-J. Chun, Y. Koike, H. Ashima, K. Kinoshita, K. Ijima, K. Fujikawa, S. Suzuki, M. Nomura, Y. Iwasawa, K. Asakura, *Chem. Phys. Lett.* **2009**, *470*, 99.

8 K. Asakura, S. Takakusagi, H. Ariga, W.-J. Chun, S. Suzuki, Y. Koike, H. Uehara, K. Miyazaki, Y. Iwasawa, *Faraday Discuss.* **2013**, *162*, 165.

9 W.-J. Chun, Y. Koike, K. Ijima, K. Fujikawa, H. Ashima, M. Nomura, Y. Iwasawa, K. Asakura, *Chem. Phys. Lett.* **2007**, *433*, 345.

10 Y.-R. Luo, Comprehensive Handbook of Chemical Bond Energies. CRC Press, **2007**, *5*, 22.

11 R. Nakamura, N. Ohashi, A. Imanishi, T. Osawa, Y. Matsumoto, H. Koinuma, Y.

Nakato, *J. Phys. Chem. B* **2005**, *109*, 1648.

12 Y. Yamamoto, K. Nakajima, T. Ohsawa, Y. Matsumoto, H. Koinuma, *Jpn. J. Appl. Phys*. **2005**, *44*, L511.

13 W.-J. Chun, Y. Tanizawa, T. Shido, Y. Iwasawa, M. Nomura, K. Asakura, *J. Synchrotron Radiat*. **2001**, *8*, 168.

14 T. Yoshida, S. Sawada, *Bull. Chem. Soc. Japan* **1976**, *49*, 3319.

15 V. K. Kaushik, *Spectrochim. Acta, Part B* **1989**, *44*, 581.

16 N. Kosugi, H. Kondoh, H. Tajima, H. Kuroda, *Chem. Phys.* **1989**, *135*, 149.

17 T. Yokoyama, N. Kosugi, H. Kuroda, *Chem. Phys.* **1986**, *103*, 101.

18 D. A. Chen, M. C. Bartelt, R. Q. Hwang, K. F. McCarty, *Surf. Sci.* **2000**, *450*, 78.

19 A. L. Ankudinov, B. Ravel, J. J. Rehr, S. D. Conradson, *Phys. Rev.* B **1998**, *58*, 7565.

20 Y. A. Kondratenko, A. A. Nikonorova, A. A. Zolotarev, M. Y. Arsent'ev, G. G. Nyanikova, V. L. Ugolkov, E. I. Sysoev, T. A. Kochina, *Inorganica Chimica Acta* **2022**, *530*, 120705.

21 T. Pai, O. Stefanczyk, K. Kumar, C. Mathonière, B. Sieklucka, S.-i. Ohkoshi, *Inorg. Chem. Front.* **2022**, *9*, 771.

22 N. D. Corona-Motolinia, B. Martínez-Valencia, L. Noriega, B. L. Sánchez-Gaytán, A. Mendoza, F. J. Meléndez-Bustamante, M. E. Castro, E. González-Vergara, *Metals* **2021**, *11*, 1541.

23 Y. Li, M. Nguyen, L. Vendier, A. Robert, Y. Liu, B. Meunier, *J. Mol. Struct*. **2022**, *1251*, 132078.

24 D. Grandjean, H. L. Castricum, J. C. van den Heuvel, B. M. Weckhuysen, *J. Phys. Chem. B* **2006**, *110*, 16892.

25 D. Grandjean, V. Pelipenko, E. D. Batyrev, J. C. van den Heuvel, A. A. Khassin, T. M. Yurieva, B. M. Weckhuysen, *J. Phys. Chem. C* **2011**, *115*, 20175.

26 Y. Tanizawa, W.-J. Chun, T. Shido, K. Asakura, Y. Iwasawa, *J. Synchrotron Radiat.* **2001**, *8*, 508.

27 J. L. DuBois, P. Mukherjee, A. M. Collier, J. M. Mayer, E. I. Solomon, B. Hedman, T. D. P. Stack, K. O. Hodgson, *J. Am. Chem. Soc.* **1997**, *119*, 8578.

Chapter 4

Structural optimization for atomic Cu dispersion on TiO_2 (110) surface premodified by amine-containing carboxylic compound with theoretical consideration

Introduction

Functionalization of surfaces is currently a prominent research topic in materials development. Recently, specifically processed hybrid materials composed of inorganic nanoparticles and organic linkers have shown extraordinary mechanical properties due to intermolecular interactions. Since the early 1990s, dye-sensitized solar cells have attracted interest by promising to be a cheap and environmentally friendly alternative to conventional semiconducting photovoltaic devices. In these two fields, as well as in photocatalysis, TiO_2 rutile functionalized with carboxylic acids serves as a prototype system.[1] Typically, the adsorbate dissociates into a carboxylate species, binding toward two adjacent undercoordinated surface Ti atoms in a bidentate manner, with an H^+ forming a hydroxyl group at an undercoordinated, protruding surface oxygen atom, known as a bridging oxygen (Figure 4-1). This holds for formic acid, acetic acid[2], benzoic acid[3], various amino acids.[4] Several factors add complexity to the adsorption process, including dissociative versus molecular adsorption, the geometric (structural) effect of

the underlying substrate, as well as the ligand effect. These factors significantly affect surface functionality and metal dispersion, motivating this study.

In the previous chapter 3, I successfully determined the structure of Cu adsorption of *o*-anthranilic acid (*o*-AA) on TiO_2(110) using PTRF-XAFS measurement. Since PTRF-XAFS provides information only about the surrounding atoms of the absorbing atom, I could determine the exact local structure of N–Cu–O but with partial structures due to several consumptions. Therefore, theoretical considerations were applied to create a more accurate modeling structure. Here, to determine the Cu adsorption of *o*-AA on TiO_2(110), several Cu adsorption configurations were modeled using density-functional theory (DFT) calculations to study the interaction between *o*-AA and the TiO_2(110) surface, supporting the geometry investigations.

Computational details

DFT calculations were performed under periodic boundary conditions using the Vienna Ab initio Simulation Package (VASP) version 5.4.1.[5, 6] The projector augmented wave (PAW) method[7-9] was adopted for calculations with spin polarization and van der Waals corrections (DFT-D3).[10] Iterative electronic relaxations are done such that energy differences (E_{diff}) between two successive steps should not exceed 10^{-5} eV. The Perdew−Burke−Ernzerhof (PBE) exchange-correlation functional was used for calculations within the generalized gradient approximation (GGA) applied for the

exchange-correlation interaction.[11] A Brillouin zone was sampled using 1×1×1 Γ-centered k-point grids for optimization and 5×5×3 Monkhorst-Pack grids for density of state (DOS) calculation, respectively. The strong onsite Coulombic interactions of the Ti2p states were corrected using the Hubbard U term method (DFT+U), and 5.0 eV was used for $U_{effective}$ (= U − J).[12] A crystal structure of bulk TiO_2 was obtained from the Materials Project database.[13] The calculated lattice constant was a=4.59 Å and c=3.00 Å, which is consistent with the computational value of a=4.59 Å and c=2.96 Å and the experimental value of a=4.58 Å and c=2.94 Å.[14] The molecular models were visualized using Chemcraft software.

TiO_2(110) slab model

Periodic TiO_2 slabs contained four Ti-O-Ti trilayers and (1 × 1) extended surface unit cells (36 Ti and 72 O atoms) as shown Figure 4-2. Atoms in the lower half of the slab were fixed at their bulk positions, and the upper half of the slab and the adsorbate were allowed to relax. These cells were large enough to ensure no interaction between adsorbate molecules in periodically repeated image cells. Thus, these calculations represented isolated adsorbate molecules rather than a monolayer. Also, a vacuum thickness of 15 Å is enough to eliminate interaction between periodic images.

Adsorption of o-AA on TiO_2(110) surface

Following literature studies of carboxylic acids, such as formic acid[15], benzoic acid[3], and other aromatic carboxylic acids on the TiO_2 surface[16], two modes of adsorption of the carboxylic group were considered: dissociative adsorption in the bridging bidentate configuration and non-dissociative adsorption. Additionally, for each of these adsorption modes of the carboxylic group, adsorption configurations were constructed where the NH_2 group was also interacting with the TiO_2(110) surface. In the past literature of *p*-aminobenzoic acid on the TiO_2(101) which has a similar geometry of *o*-anthranilic acid (*o*-AA), the bidentate mode is most likely bridging neighboring Ti_{5c} in the [010] direction.[17] In this same manner, *o*-AA also indicated bidentate adsorption behavior on the Ti_{5c} site (Figure 4-3). Based on the calculation flow, adsorption of *o*-AA on the TiO_2(110) surface can be described as involving the following three consecutive steps: (a) dissociate hydrogen from carboxylic acid (b) diffuse hydrogen to near bridged oxygen (O_{2c}) (c) chemisorption of the *o*-AA on the surface as bidentate form. Note that for the charge valence of the adsorption of *o*-AA on the TiO_2(110) surface, the dissociated hydrogen from carboxylic acid is placed on the near bridged oxygen on the Ti_{5c} site, however, the actual position is hard to assign and explain. After calculation screening the various positions of hydrogen on the TiO_2(110) surface, set the most stable position, and set the location for further calculations.

Structural optimization of Cu/o-AA/TiO_2(110)

Before the optimization of the initial structure for DFT, the position of the *o*-AA molecule/TiO_2(110) is conducted from the model structure determined by PTRF-XAFS measurement. According to the change of initial positions of Cu atom, the optimization of Cu/*o*-AA/TiO_2(110) was carried out. The initial positions of the Cu atom are shown in Figure 4-4. The relative energy of the Cu adsorption site is determined by the equation 4-1 as

$$E_r = E_{site\_x} - E_{site\_b} \qquad \text{(Equation 4-1)}$$

The most unstable site is the (b) hollow site on the surface, therefore I set the standard value for the calculation of relative energy (Table 4-1). As a result of the calculation, the initial structure where Cu was positioned ontop at Ti_{5c} indicated the most stable structure.

Also, adsorption energies E_{ads} of optimized structures were calculated as

$$E_{ads} = E_{slab+oAA} - E_{slab} - E_{oAA} \qquad \text{(Equation 4-2)}$$

where E_{slab} is the energy of the TiO_2 slab, E_{oAA} is the energy of the isolated *o*-AA molecule in the gas phase, and $E_{slab+oAA}$ is the energy of the surface-adsorbate system. Negative values of adsorption energies correspond to favorable adsorption. The most favorable structure is the (a) ontop at Ti_{5c}. The adsorption energy gap between the most stable (ontop at Ti_{5c}) and most unstable (hollow site) position is 0.8 eV.

Figure 4-6 shows the detailed 3D structure of Cu/*o*-AA/TiO_2(110) by DFT

calculations. The first thing I can decide from the DFT is the position of two hydrogens contained in *o*-AA could be determined which formed tetrahedral local geometry of nitrogen atom (the angle of H−N−H was 107 º). In addition, on the determined model from PTRF-XAFS measurement in chapter 3 (abbreviated $Model_{exp}$), the *o*-AA molecule was placed perpendicular (88 º) to the surface and tilted by 21 º with respect to the surface normal. However, from the DFT optimization, *o*-AA molecules were more lying down to the surface (66 º) and more twisted 25 º with respect to the surface normal because hydrogen showed a tendency to be closer to the oxygen of carboxylate forming hydrogen bonding. Therefore, the bond distance of O··H−N showed 0.180 nm which was consistent with a typical hydrogen bonding distance of H−O (0.180-0.210 nm). [18-20]

The Cu–O and the Cu–N bond distances were 0.185 nm and 0.193 nm, respectively, which were slightly shorter than the $Model_{exp}$ (0.193 nm and 0.215 nm). The bond distance of Ti–O bonded with the Cu atom was 0.198nm which is longer than another Ti–O bond (0.188 nm). In the DFT calculation, because the first TiO_2 trilayer is relaxed, therefore, each surface Ti–O is possible to move position and change bond distance. The Cu–N and Cu–O bond angles to the surface normal (to the [110] direction) were 53° and 47°, respectively, which indicated the local structure of the N–Cu–O bonding motif is more perpendicular than that of $Model_{exp}$ (61 ° and 43 °). Also, the Cu–N and Cu–O bonds were oriented 32° and 38° to the $[1\bar{1}0]$ direction, showing a mismatch compared with $Model_{exp}$(49 ° and 61 °) In addition, The N–Cu–O bond angle

was estimated to be 172°, which was more linear found in $Model_{exp}$ (162 °). Subsequently, Bader atomic charge and electron density differences were analyzed to clarify the interactions between the Cu atom and the surfaces.[21-24] From the DFT calculation, the charge distribution can be approximated by the calculation of Bader's atomic charge, indicating the total electronic charge of an atom (Figure 4-7). The charge distribution can be used to determine multipole moments of interacting atoms or molecules. The Cu is positively charged around +0.61 |e| in the cationic state and N is negatively charged around -1.21 |e| in the anionic state.

Conclusion

In this chapter, the structure of Cu/*o*-AA/TiO_2(110) was determined by DFT calculation as a theoretical method. Compared with a proposed model from PTRF-XAFS measurement, the *o*-AA molecule was lying down to the surface and more twisted with respect to the surface normal because of the hydrogen bonding between H of *o*-AA and O of carboxylate. In addition, the position of H is determined by forming the tetrahedral geometry of NH_2. The cationic state of the Cu atom was also confirmed by the calculation.

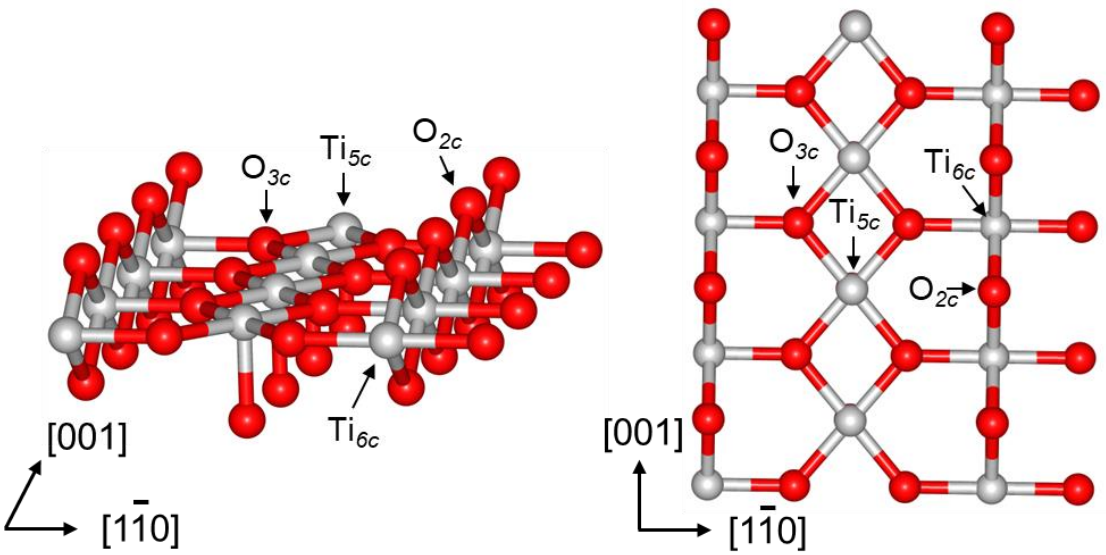

Figure 4-1. Surface of TiO_2(110).

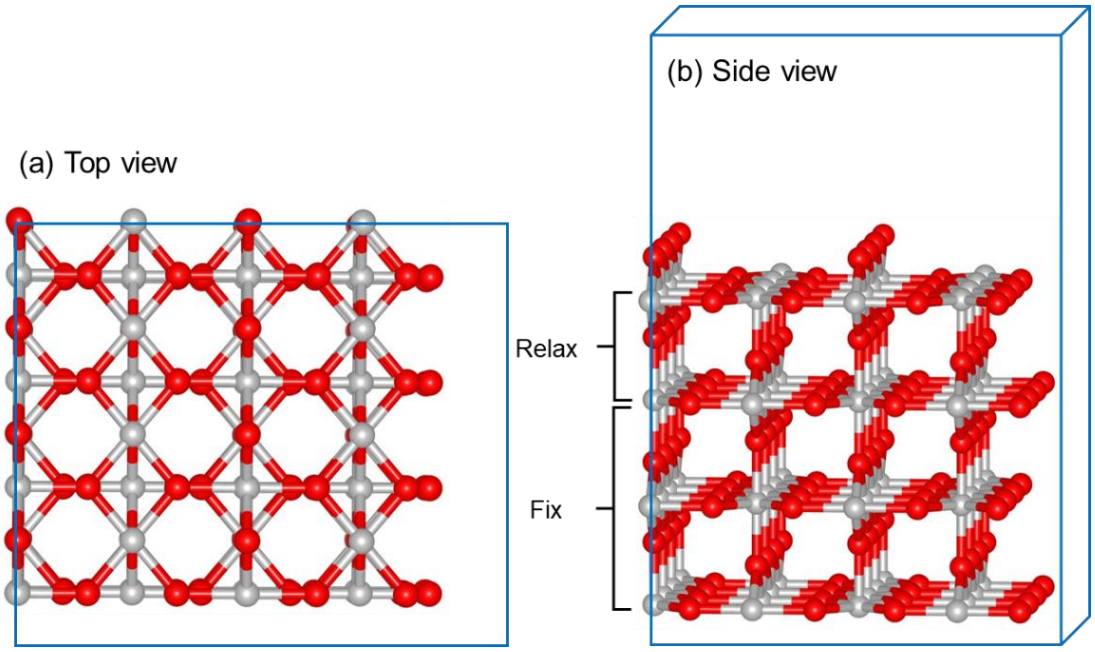

Figure 4-2. TiO_2(110) slab structure (a) top view and (b) side view. The light gray and red colors indicate Ti and O atoms, respectively.

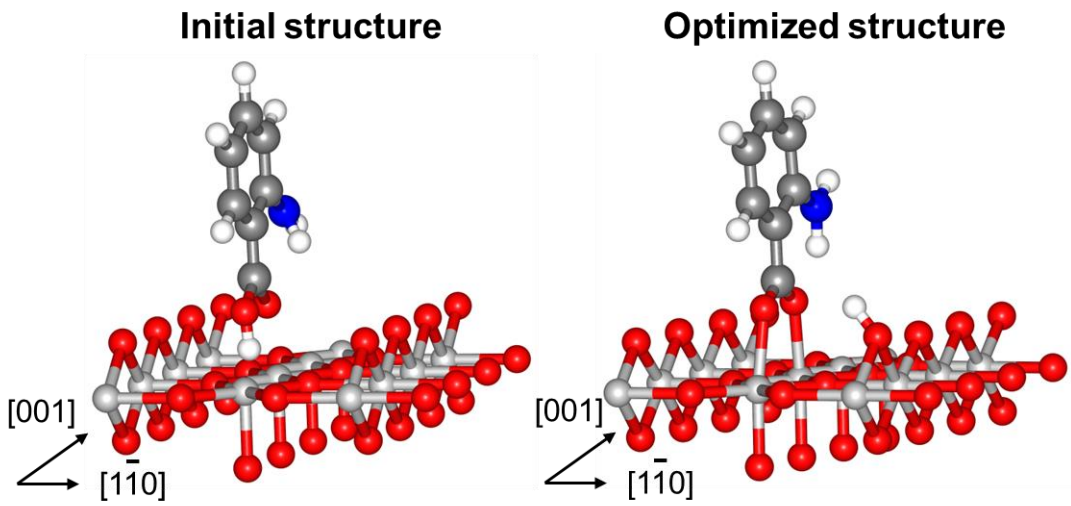

Figure 4-3. Bidentate adsorption structure of dissociated *o*-anthranilic acid on TiO_2(110) surface. The white, dark gray, red, blue, and light gray colors indicate H, C, O, N, and Ti atoms, respectively.

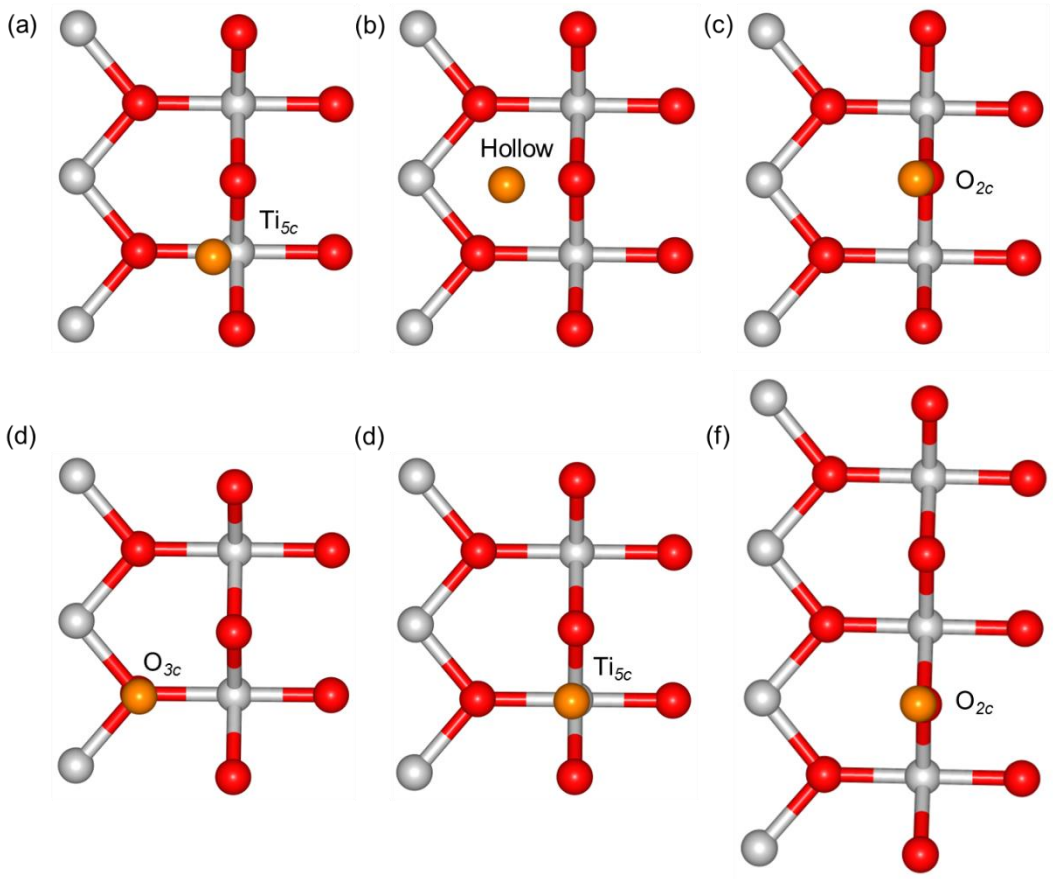

Figure 4-4. Initial positions of Cu atoms (a) ontop at Ti_{5c} (b) hollow site (c) ontop at O_{2c} (d) ontop at O_{3c} (e) ontop at Ti_{6c} (f) ontop at O_{2c}. The orange, red, and light gray colors indicate Cu, O, and Ti atoms, respectively.

Table 4-1. Results of optimization and adsorption energy of Cu/*o*-AA/TiO_2(110) for DFT calculations. The Cu position follows (a) ontop at Ti_{5c} (b) hollow site (c) ontop at O_{2c} (d) ontop at O_{3c} (e) ontop at Ti_{6c} (f) ontop at O_{2c}.

	a	b	c	d	e	f
Optimized Energy (eV)	-1572.15	-1571.35	-1571.48	-1571.51	-1571.55	-1571.55
Relative Energy (eV)	-0.89	0	-0.13	-0.16	-0.20	-0.19

	a	b	c	d	e	f
E_{ads}(eV)	-4.08	-3.28	-3.41	-3.44	-3.48	-3.48

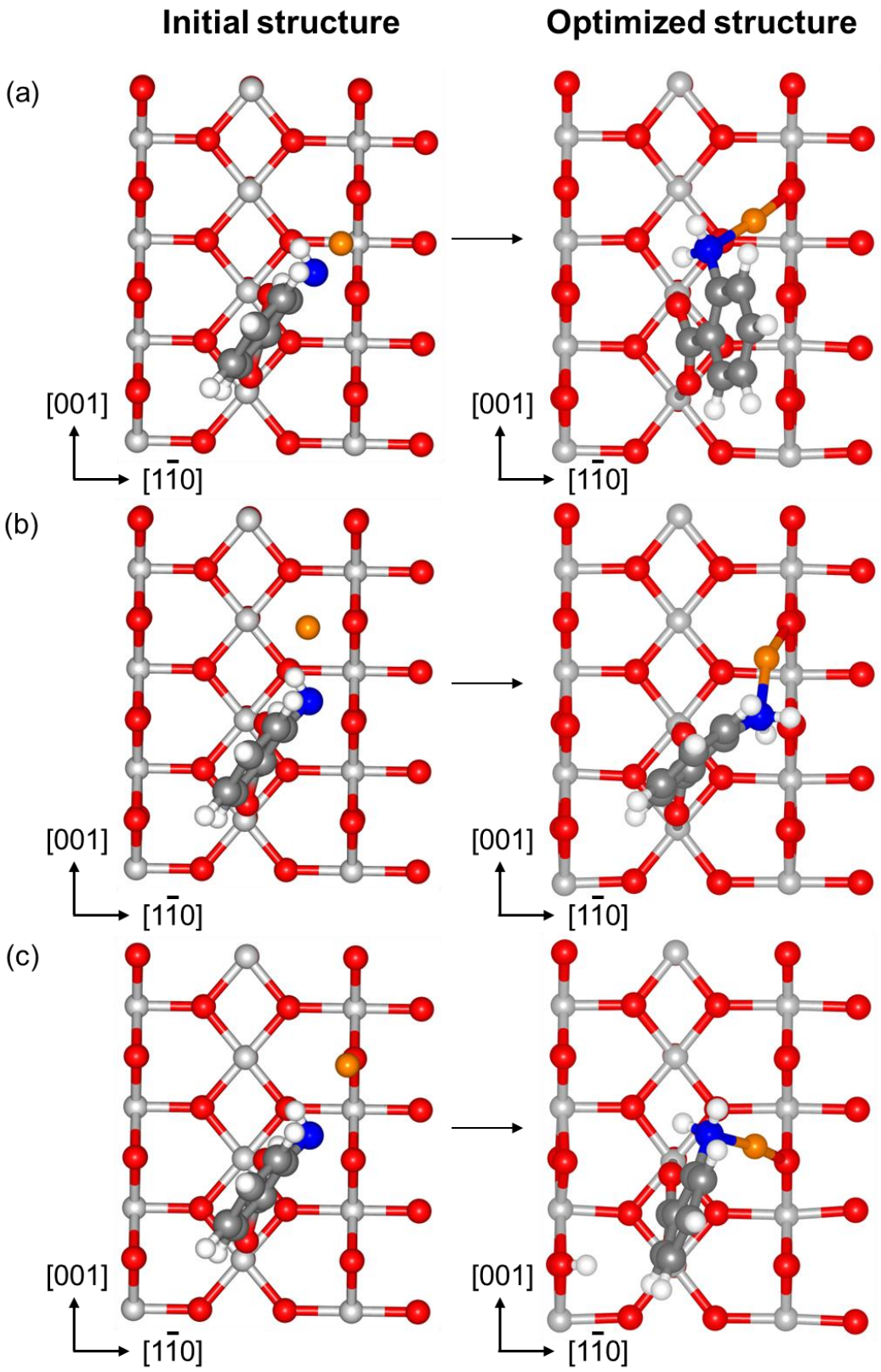
Initial structure
Optimized structure
(a)
(b)
(c)
[001]
[1$\bar{1}$0]
[001]
[1$\bar{1}$0]
[001]
[1$\bar{1}$0]
[001]
[1$\bar{1}$0]
[001]
[1$\bar{1}$0]
[001]
[1$\bar{1}$0]

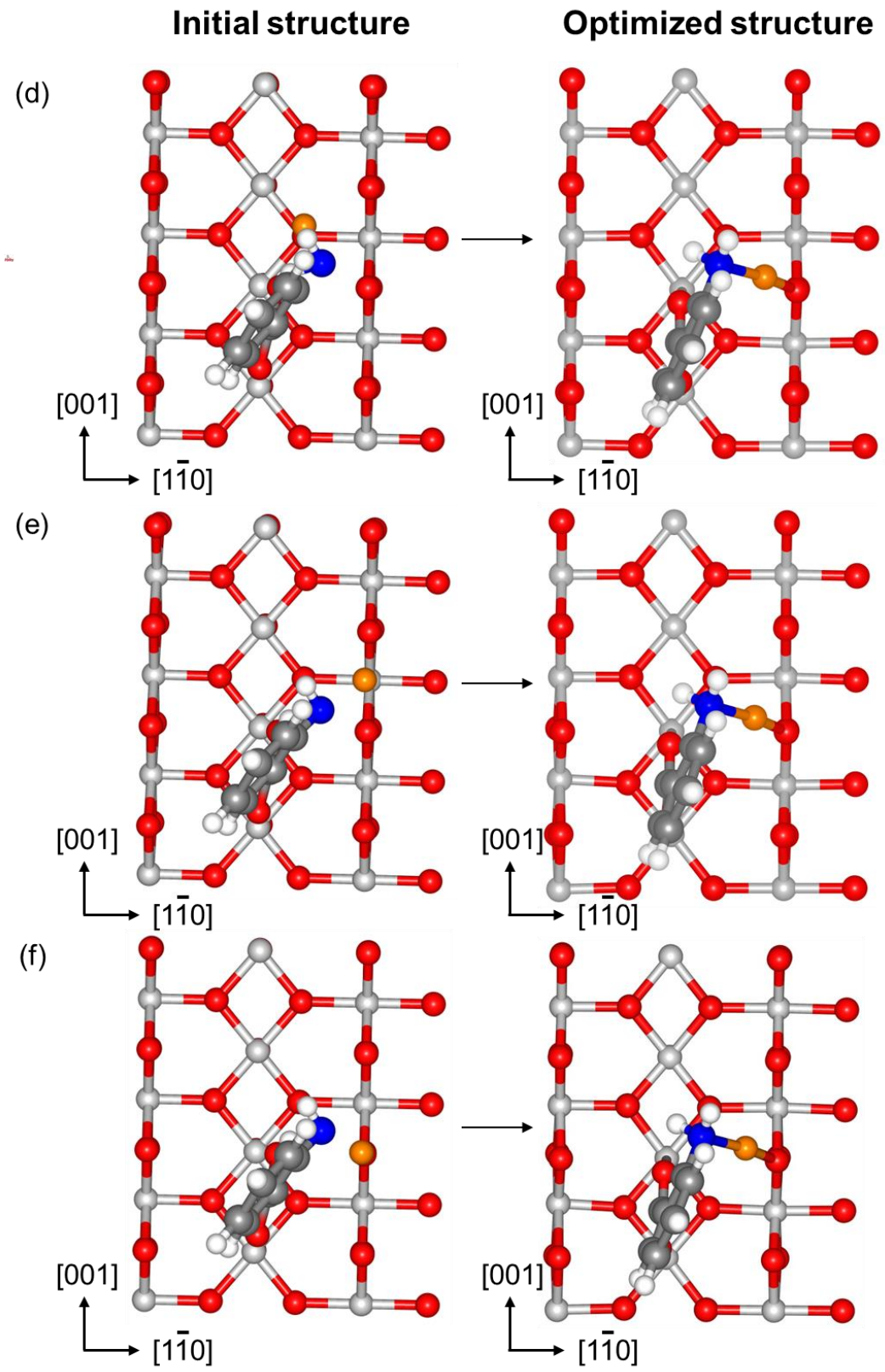

Figure 4-5. Atomic Cu dispersion of on TiO_2(110) surface modified *o*-AA which initial

structures (left) and optimized structures from DFT calculations (right); initial positions of Cu are (a) ontop at Ti_{5c} (b) hollow site (c) ontop at O_{2c} (d) ontop at O_{3c} (e) ontop at Ti_{6c} (f) ontop at O_{2c}. The white, dark gray, orange, red, blue, and light gray colors indicate H, C, Cu, O, N, and Ti atoms, respectively.

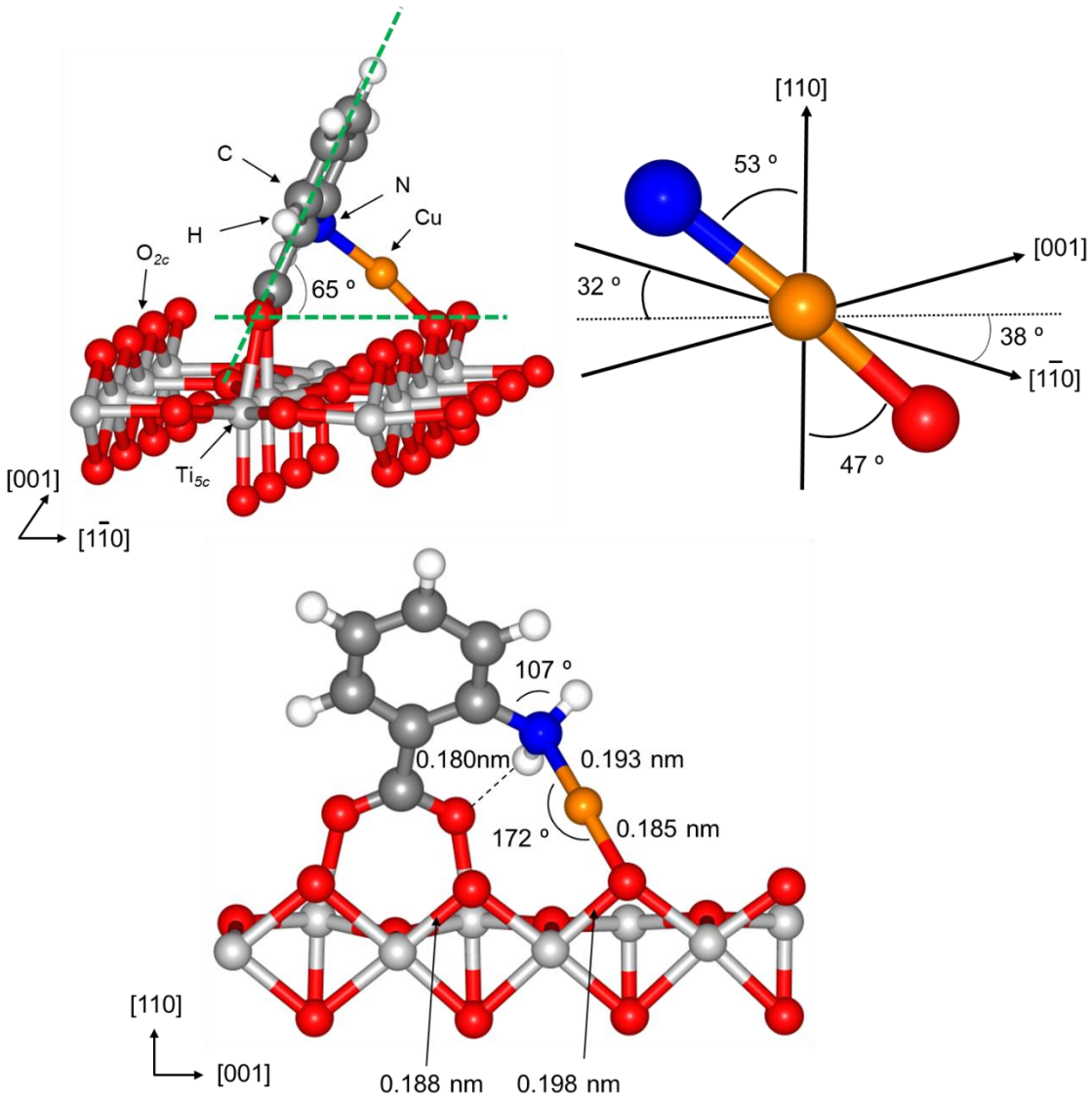

Figure 4-6. Detailed 3D structure of Cu/*o*-AA/TiO_2(110) from optimization of DFT calculations.

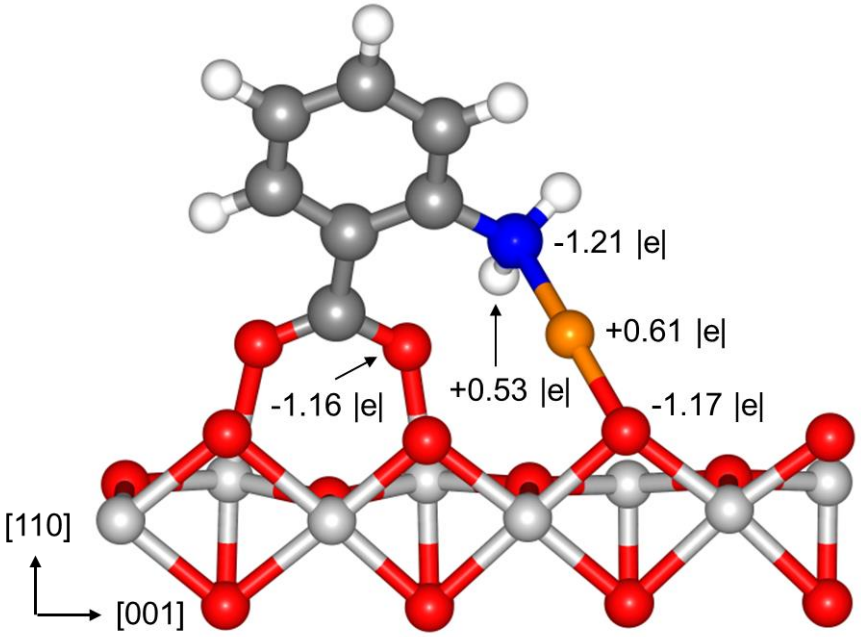

Figure 4-7. Bader atomic charge information of Cu/*o*-AA/TiO_2(110).

Reference

1 D. C. Grinter, T. Woolcot, C.-L. Pang, G. Thornton, *The Journal of Physical Chemistry Letters* **2014**, *5*, 4265.

2 J. Tao, T. Luttrell, J. Bylsma, M. Batzill, *The Journal of Physical Chemistry C* **2011**, *115*, 3434.

3 M. Buchholz, M. Xu, H. Noei, P. Weidler, A. Nefedov, K. Fink, Y. Wang, C. Wöll, *Surface Science* **2016**, *643*, 117.

4 C. L. Pang, R. Lindsay, G. Thornton, *Chemical Society Reviews* **2008**, *37*, 2328.

5 G. Kresse, J. Furthmüller, *Computational Materials Science* **1996**, *6*, 15.

6 G. Kresse, J. Hafner, *Physical Review B* **1993**, *47*, 558.

7 G. Kresse, D. Joubert, *Physical Review B* **1999**, *59*, 1758.

8 O. Bengone, M. Alouani, P. Blöchl, J. Hugel, *Physical Review B* **2000**, *62*, 16392.

9 P. E. Blöchl, *Physical Review B* **1994**, *50*, 17953.

10 S. Grimme, J. Antony, S. Ehrlich, H. Krieg, *The Journal of Chemical Physics* **2010**, *132*,

11 J. P. Perdew, K. Burke, M. Ernzerhof, *Physical Review Letters* **1996**, *77*, 3865.

12 T. T. Thoa, H. Van Hung, N. T. M. Hue, *Vietnam Journal of Chemistry* **2022**, *60*, 183.

13 A. Jain, S. P. Ong, G. Hautier, W. Chen, W. D. Richards, S. Dacek, S. Cholia, D. Gunter, D. Skinner, G. Ceder, K. A. Persson, *APL Materials* **2013**, *1*,

14 T. T. Thoa, T. T. Nguyen, H. Van Hung, N. T. M. Hue, *Vietnam Journal of Chemistry* **2023**, *61*, 563.

15 K.-i. Fukui, H. Onishi, Y. Iwasawa, *Chemical Physics Letters* **1997**, *280*, 296.

16 C. Lun Pang, R. Lindsay, G. Thornton, *Chemical Society Reviews* **2008**, *37*, 2328.

17 A. G. Thomas, M. J. Jackman, M. Wagstaffe, H. Radtke, K. Syres, J. Adell, A. Lévy, N. Martsinovich, *Langmuir* **2014**, *30*, 12306.

18 R. Taylor, O. Kennard, *Accounts of Chemical Research* **1984**, *17*, 320.

19 H.-G. Korth, M. I. de Heer, P. Mulder, *The Journal of Physical Chemistry A* **2002**, *106*, 8779.

20 N. Madusanka, M. D. Eddleston, M. Arhangelskis, W. Jones, *Acta Crystallographica Section B* **2014**, *70*, 72.

21 G. Henkelman, A. Arnaldsson, H. Jónsson, *Computational Materials Science* **2006**, *36*, 354.

22 E. Sanville, S. D. Kenny, R. Smith, G. Henkelman, *Journal of Computational Chemistry* **2007**, *28*, 899.

23 W. Tang, E. Sanville, G. Henkelman, *Journal of Physics: Condensed Matter* **2009**, *21*, 084204.

24 M. Yu, D. R. Trinkle, *The Journal of Chemical Physics* **2011**, *134*, 064111.

Chapter 5

Reconstruction for the atomic Cu dispersion on TiO_2(110) surface premodified by amine-containing carboxylic compound combined with experimental and theoretical methods

Introduction

X-ray absorption spectroscopy (XAS)[1, 2] and computational chemistry methods, such as density functional theory (DFT)[3,4] for structure calculations, are highly complementary tools for elucidating chemical and structural information of metal species. Extended X-ray absorption fine structure (EXAFS) is particularly sensitive to changes in bond distance, serving as a critical metric for narrowing down the type of coordinating ligand, coordination number, and, in some cases, coordination geometry. This technique provides a three-dimensional structure of clusters highly dispersed on a single crystal surface using the polarization dependence of EXAFS amplitude. For K and L_1 absorption edges,

$$\chi_{obs}(k) = \sum_i 3\cos^2\theta_i \cdot \chi_i(k) \qquad \text{(Equation 5-1)}$$

where θ_i is an angle between the polarization vector $\vec{E}$ of the incident X-ray and the

bond vector.

Both EXAFS and DFT calculations can obtain significant atomic-scale resolution information of the local structure around the site of interest. However, structural information provided by EXAFS of the metal site is typically limited to below 5 Å around the metal center.[5] This volume is sufficient to encompass the primary coordinating ligands, making it a useful scale for generating structures for DFT calculations. Furthermore, EXAFS serves as a chemically and structurally sensitive probe, enhancing the information available for DFT calculation. However, EXAFS curve fitting especially with multiple scattering contributions from outer shell atoms, necessitates three-dimensional structural information, which can be obtained from small molecules or optimized structures calculated by DFT. DFT calculations can be employed to test alternate structures and chemical forms, providing thermodynamic information such as energy, enthalpies, and entropic components. Therefore, they are valuable in building model structures that fit well with experimental data. It's important to note that while EXAFS can provide bond distances accurate to ±0.002 nm, DFT calculations are typically regarded as accurate to ±0.005 nm, depending on the selected functions and basis set.[6] It's worth noting that, in some cases, the accuracies of DFT calculations may surpass this estimate, providing significantly better results depending on the computational parameters. It is also possible that small molecule crystal structures can provide insight to supplement EXAFS and DFT, however, they can be mismatched owing to the crystal

packing forces and other factors. Therefore, it is expected that more accurate structural decisions will be realized by considering both methods from various perspectives.

In this chapter, I propose a reconstructed structure of Cu dispersion on the TiO_2(110) surface, premodified by an amine-containing carboxylic compound. This suggestion is based on findings from PTRF-XAFS and DFT calculations, as presented in previous chapters 3 and 4.

EXAFS fitting analysis by FEFF code

The EXAFS analysis was carried out as described before composed of elucidation of EXAFS oscillation, normalization, and real space fitting. The EXAFS spectra are elucidated using spline smoothing with Cook-Sayer criteria for the background removal.[7] The oscillation was normalized by an edge height with its energy dependence was expressed by a Victoreen equation. The obtained spectrum was directly compared to a calculated EXAFS oscillation determined by FEFF8. FEFF code was developed by J. J. Rehr, *et al*.[8, 9] In FEFF code, the ab initio multiple scattering calculations of XAFS are carried out and yield scattering amplitude and phases for each path. In this thesis, FEFF8.20 was applied for the calculation. Based on the result of DFT optimization, the positions of each atom were obtained as an XYZ file to prepare an input file for calculation by FEFF code. The example of input file is shown in Table 5-1. For the FEFF simulation applied from the position of DFT calculation, each polarization

vector should be determined because of the relaxation of the first trilayer of the TiO_2(110) surface. Such interaction between the adsorption molecule and surface is possible to cause a difference compared to the fitting result of PTRF-XAFS measurement. The defined R-value can judge the matching for the experimental oscillation data and the calculated result from the FEFF code. The goodness of fitting can be indicated using *R* value which is expressed by the following equation.

$$R = \sqrt{\frac{1}{N}\sum_k \frac{(\chi_{obs}(k) - \chi_{cal}(k))^2}{\varepsilon(k)^2}} \quad \text{(Equation 5-2)}$$

Reconstruction for the atomic Cu dispersion on TiO_2(110) premodified with o-anthranilic acid

In Chapter 3, the structure of atomic Cu dispersion on TiO_2 premodified with *o*-anthranilic acid (denoted Cu/*o*-AA/TiO_2(110)) was successfully determined through PTRF-XAFS measurement (Figure 5-1). The local model of Cu surroundings, especially the N−Cu−O bonding motif, was precisely identified. The Cu–N and Cu–O bond distances were determined to be 0.215 nm and 0.193 nm, respectively. Additionally, the Cu–N and Cu–O bonds were oriented 49° and 61° to the $[1\bar{1}0]$ direction. Furthermore, the Cu–N and Cu–O bond angles to the surface normal ([110] direction) were measured at 61° and 43°, respectively. The N–Cu–O bond angle was estimated to be 162°, suggesting that Cu was in a monovalent state.

However, a question arose from the PTRF-EXAFS spectra of the Cu/*o*-AA/TiO_2 (110) (Figure 5-2). In the spectra indicating the polarization dependence of EXAFS amplitude, the intensities of [001] and $[1\bar{1}0]$ were similar, but the intensity of [110] was almost twice than that of [001] and $[1\bar{1}0]$. According to the equation 5-1, the bond angle adsorbing atom (copper in this study) between neighboring atom (nitrogen in this study) should be perpendicular compared to the previously proposed model. Therefore, a reconstruction of the defined structure is deemed necessary.

Figure 5-3 illustrates a structure of Cu/*o*-AA/TiO_2 (110) based on the DFT optimization, as I explained in Chapter 4. The Cu–N and Cu–O bond distances were determined to be 0.193 nm and 0.185 nm, respectively. The Cu–N and Cu–O bonds were oriented at 32° and 38° to the $[1\bar{1}0]$ direction, with the Cu–N and Cu–O bond angles to the surface normal ([110] direction) were 53° and 47°, respectively. The N–Cu–O bond angle was estimated to be 172°. FEFF simulation was performed using atomic positions obtained from the DFT calculation. Upon comparing the observed PTRF-EXAFS spectra of Cu/*o*-AA/TiO_2(110) with those calculated by the FEFF code in three different polarization directions, a close match was observed except for E//[001], where the *R-value* was >1 (determined by equation 5-2). Hence, the structure of Cu/*o*-AA/TiO_2(110) needs revision.

Based on the DFT calculation, I revised the Cu/*o*-AA/TiO_2(110) structure, as shown in Figure 5-4. In this revised model, the Cu–N and Cu–O bond distances were

maintained at 0.215 nm and 0.193 nm, respectively, consistent with the PTRF-XAFS measurement results. The Cu–N and Cu–O bonds were oriented at 41° and 45° to the $[1\bar{1}0]$ direction, in alignment with the PTRF-EXAFS amplitude close to 45° to [001] and $[1\bar{1}0]$ directions. he Cu–N and Cu–O bond angles to the surface normal ([110] direction) were 51° and 47° based on the DFT calculation. FEFF simulation was performed on the modified structure of Cu/*o*-AA/TiO_2(110). Upon comparing the observed PTRF-EXAFS spectra of Cu/*o*-AA/TiO_2(110) with those calculated by the FEFF code in three different polarization directions, a good agreement was observed with the observed spectra in all three directions below R=1. Therefore, it can be concluded that the revised structure of Cu/*o*-AA/TiO_2(110) fits well with the experimental data.

Conclusion

In this chapter, I explored the synergy of experimental measurement (PTRF-EXAFS) and theoretical calculation (DFT) methods, aiming to enhance our understanding of atomic-scale resolution information. The summary of local structure information is represented in Figure 5-5. The reconstructed structure for Cu dispersion on the TiO_2(110) fits well with the experimental data, underscoring the importance of an integrated approach for precise structural determination. This study emphasizes the potential for advancements in comprehending complicated surface structures through the utilization of diverse approaches.

Table 5-1. Input file for EXAFS oscillation by FEFF code.

```
* This feff.inp file generated by ATOMS, version 2.50
* ATOMS written by and copyright (c) Bruce Ravel, 1992-1999

* -- * -- * -- * -- * -- * -- * -- * -- * -- * -- * -- * -- * -- * -- *
*      total mu =      725.4 cm^-1, delta mu =      610.0 cm^-1
*      specific gravity = 12.006, cluster contains   55 atoms.
* -- * -- * -- * -- * -- * -- * -- * -- * -- * -- * -- * -- * -- * -- *
*      mcmaster corrections:  0.00020 ang^2 and  0.770E-07 ang^4
* -- * -- * -- * -- * -- * -- * -- * -- * -- * -- * -- * -- * -- * -- *

TITLE   oAA_TiO2_Cu_DFT

EDGE      K
S02       0.93

*         pot    xsph  fms   paths genfmt ff2chi
CONTROL  1     1     1     1     1     1
PRINT    1     0     0     0     0     3

*         r_scf   [ l_scf  n_scf  ca ]
*SCF      6.05142     0     15     0.1

*         ixc  [ Vr  Vi ]
* EXCHANGE  0      0   0

EXAFS    20
RPATH    10

*         kmax  [ delta_k  delta_e ]
*XANES     4.0     0.07     0.5
*         r_fms     [ l_fms ]
*FMS       6.05142    0
*
*RPATH     0.10000
*         emin  emax  resolution
*LDOS      -20    20   0.1

POTENTIALS
*   ipot   z [ label   l_scmt  l_fms  stoichiometry ]
    0   29    Cu
    1   7     N
    2   8     O

NLEG        4

*CRITERIA     4.00     2.50

*DEBYE        300.00   340.00

CORRECTION  16.0  0.0

SIG2  0.0049

POLARIZATION  -3.03  0.007  -0.017

ATOMS
0    0    0    0  Cu
0.12  -1.207  1.645  1  N
-1.745  0.392  -1.347  2  O

END
```

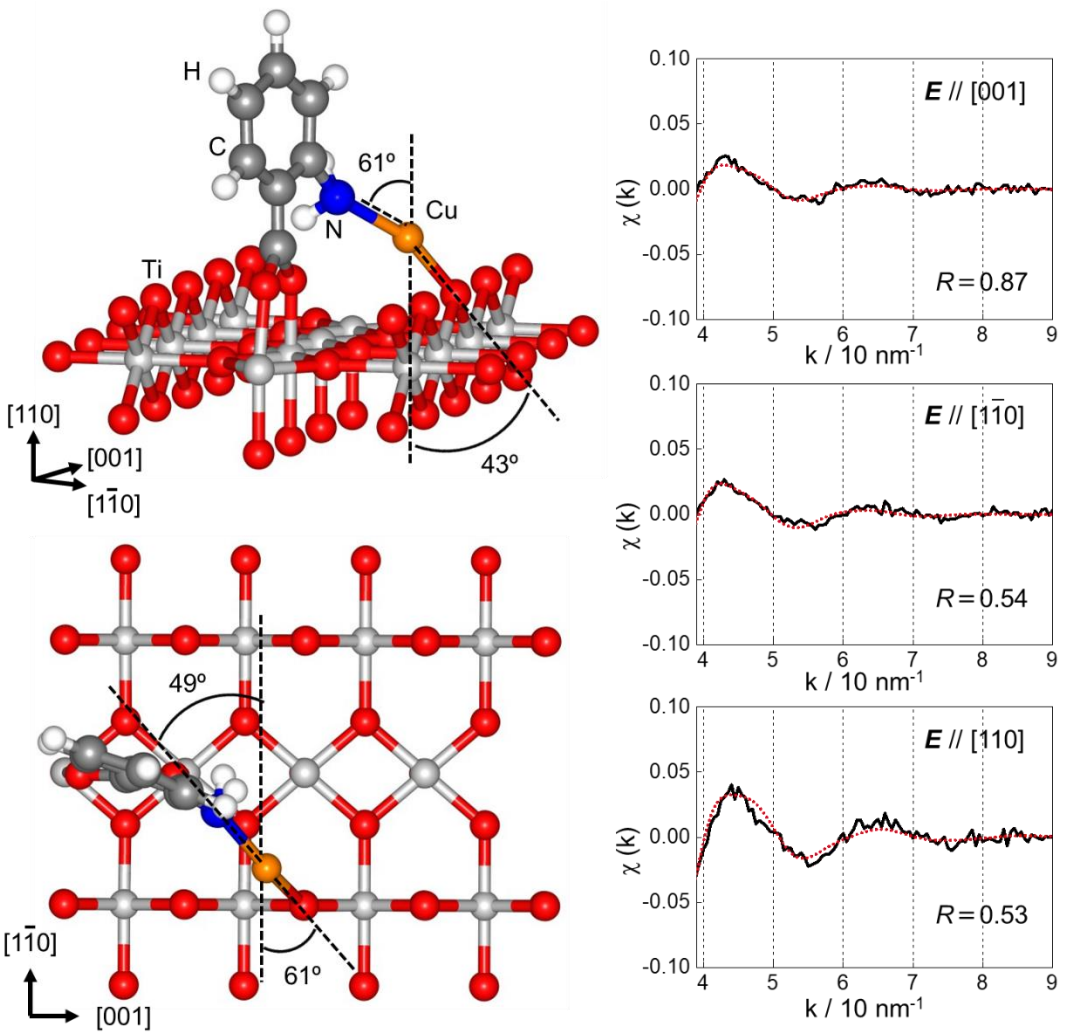

Figure 5-1. Model structure of Cu/*o*-AA/TiO_2(110) determined by experimental method as shown in Chapter 3. Comparison between observed PTRF-EXAFS spectra of Cu/*o*-AA/TiO_2(110) surface (black solid lines) and those calculated by FEFF code (red dotted lines) in three different polarization directions.

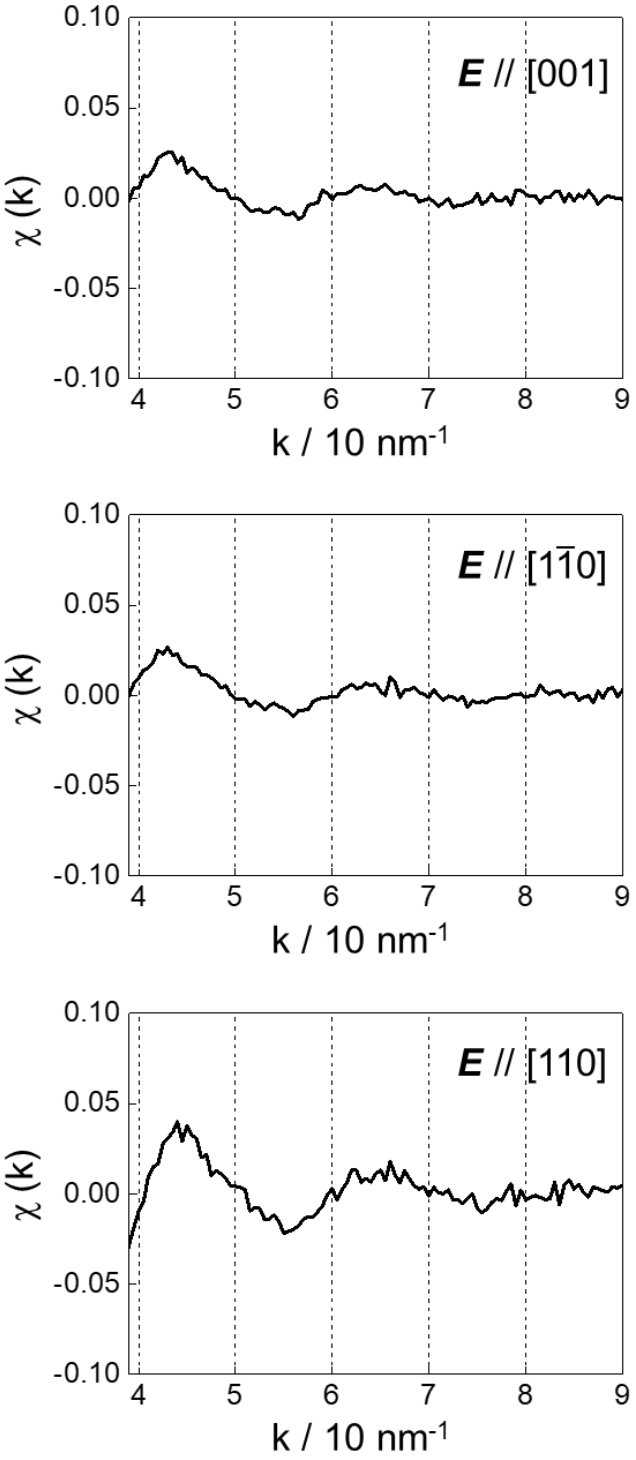

Figure 5-2. Cu K-edge PTRF-EXAFS spectra of Cu/*o*-AA/TiO_2(110) were obtained in three different polarization directions.

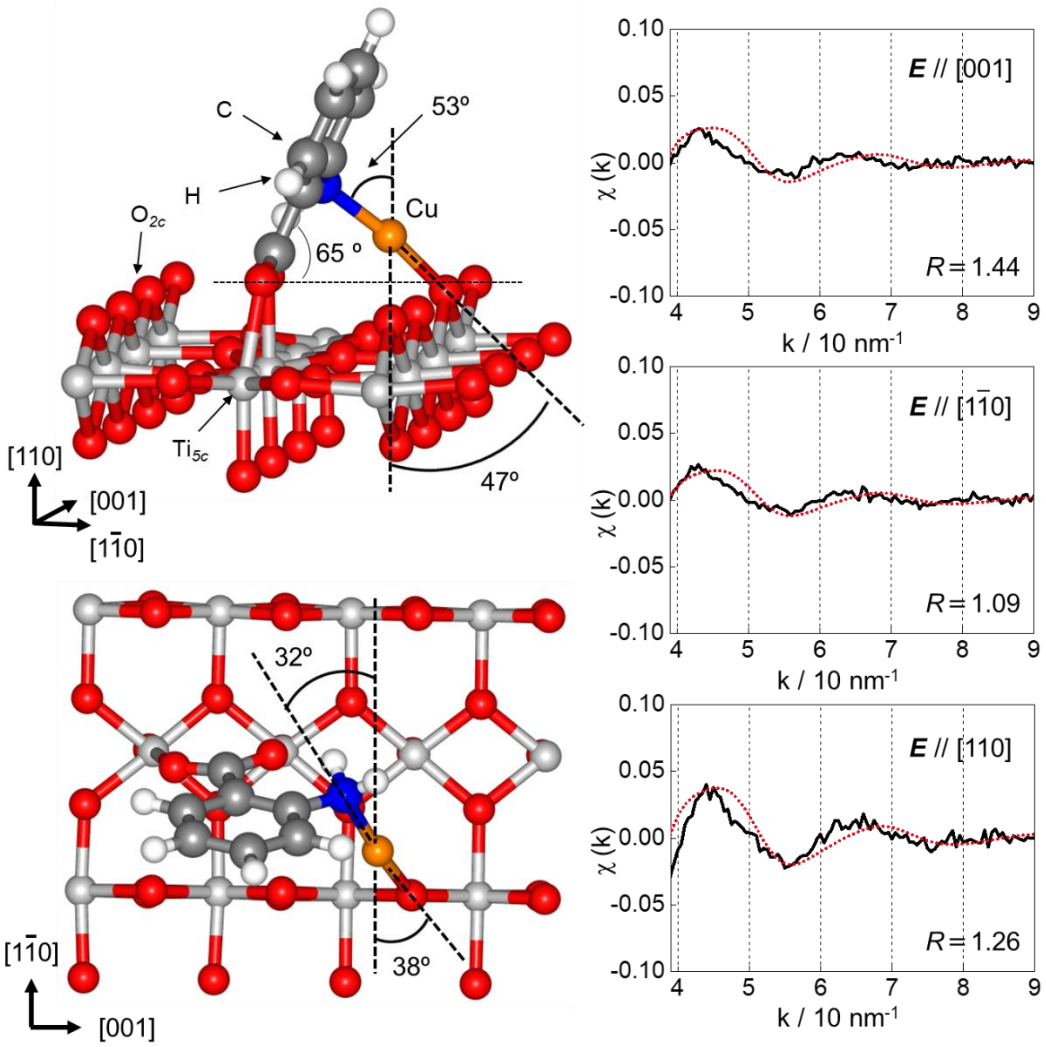

Figure 5-3. Model structure of Cu/*o*-AA/TiO_2(110) determined by theoretical method as shown in chapter 4. Comparison between observed PTRF-EXAFS spectra of Cu/*o*-AA/TiO_2(110) surface (black solid lines) and those calculated by FEFF code (red dotted lines) in three different polarization directions.

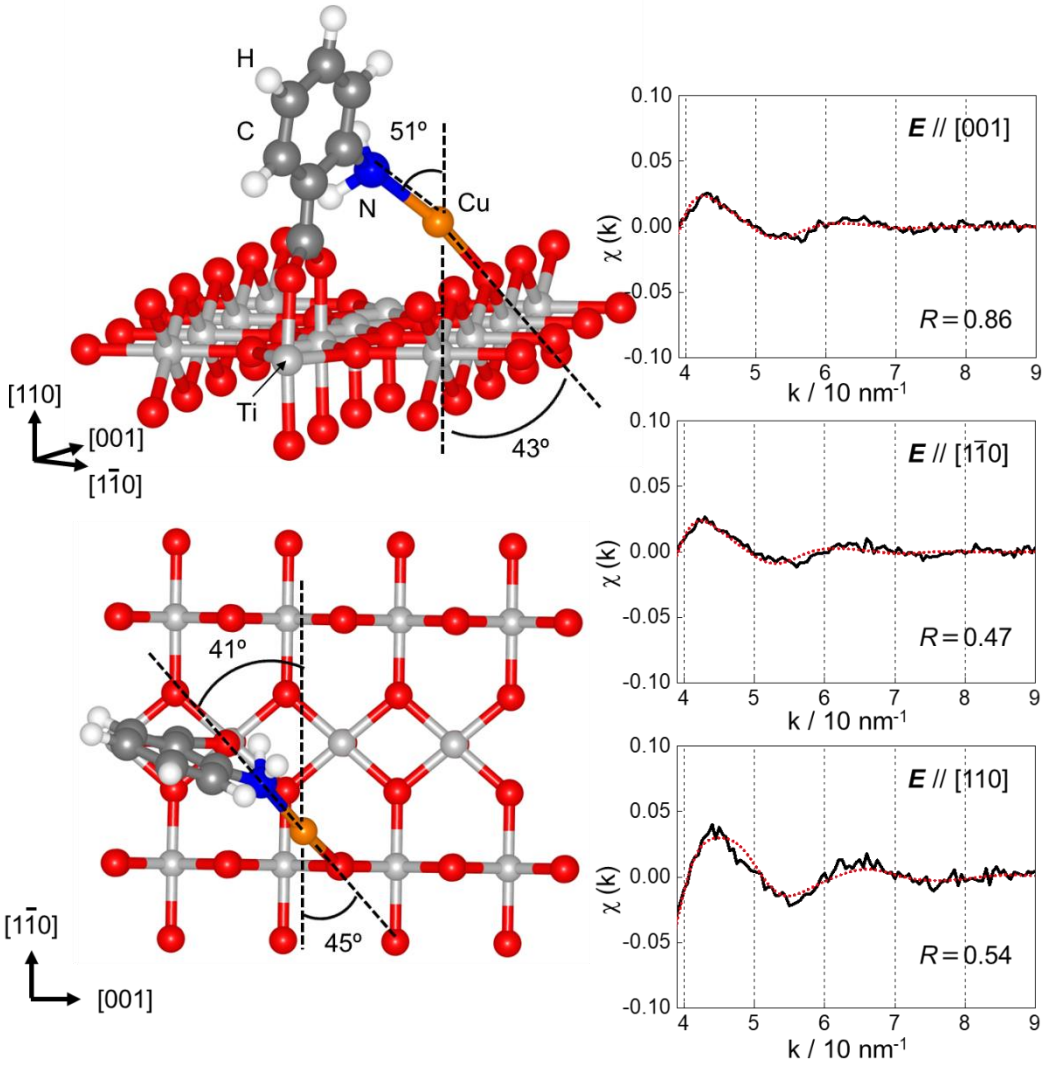

Figure 5-4. Revised model structure of Cu/*o*-AA/TiO_2(110) combined with experimental and theoretical methods. Comparison between observed PTRF-EXAFS spectra of Cu/*o*-AA/TiO_2(110) surface (black solid lines) and those calculated by FEFF code (red dotted lines) in three different polarization directions.

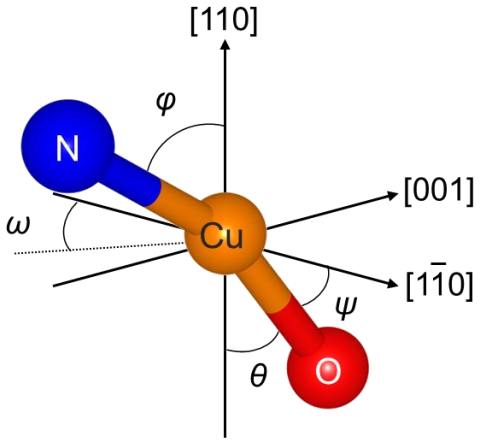

model	R(Cu–N)	R(Cu–O)	To [110]		To [1$\bar{1}$0]		∠ N–Cu–O
			∠ Cu–N	∠ Cu–O	∠ Cu–N	∠ Cu–O	
PTRF-EXAFS	0.215nm	0.193nm	61°	43°	49°	61°	162°
DFT	0.193nm	0.185nm	53°	47°	32°	38°	172°
Reconstructed	0.215nm	0.193nm	51°	43°	41°	45°	171°

Figure 5-5. Local structure information of Cu/*o*-AA/TiO_2(110).

References

1 J. Singh, C. Lamberti, J. A. van Bokhoven, *Chemical Society Reviews* **2010**, *39*, 4754.

2 C. Lamberti, J. A. van Bokhoven, in *X-Ray Absorption and X-Ray Emission Spectroscopy*, **2016**, pp. 351.

3 P. Hohenberg, W. Kohn, *Physical Review* **1964**, *136*, B864.

4 W. Kohn, L. J. Sham, *Physical Review* **1965**, *140*, A1133.

5 S. P. Cramer, K. O. Hodgson, E. I. Stiefel, W. E. Newton, *Journal of the American Chemical Society* **1978**, *100*, 2748.

6 J. A. Qiu, H. L. Wilson, M. J. Pushie, C. Kisker, G. N. George, K. Rajagopalan, *Biochemistry* **2010**, *49*, 3989.

7 J. Cook Jr, D. Sayers, *Journal of Applied Physics* **1981**, *52*, 5024.

8 J. J. Rehr, R. C. Albers, *Reviews of Modern Physics* **2000**, *72*, 621.

9 J. J. Rehr, J. J. Kas, M. P. Prange, A. P. Sorini, Y. Takimoto, F. Vila, *Comptes Rendus Physique* **2009**, *10*, 548.

Chapter 6

General conclusion

Isolated atoms on an oxide support display unique catalytic activity, defining them as single-atom catalysts (SACs). SACs, sought after for their high catalytic efficiency and cost-effectiveness with precious metals, are typically obtained by immobilizing metal species on oxide surfaces via surface hydroxyl groups or linker molecules, establishing strong interactions with both the metal species and the support. Consequently, the geometrical and electronic properties of the single atom are primarily influenced by the local coordination environment around the atom. Determining this local coordination environment is crucial for understanding the catalytic properties of SACs.

Conventional SACs often involve metal species highly dispersed on polycrystalline oxide powders with microporous structures, making it challenging to precisely determine the local coordination environment. In my research, I achieved high atomic dispersion of copper by premodification of the surface with organic linker molecules, using a single-crystalline oxide as a support.

In Chapter 3, atomic dispersed Cu was prepared through the premodification of *o*-anthranilic acid on a TiO_2(110) surface (Cu/*o*-AA/TiO_2(110)). Utilizing Polarized Total Reflection X-ray Fluorescence Absorption Fine Structure (PTRF-XAFS) measurement,

the Cu/*o*-AA/TiO_2(110) structure was determined, incorporating a novel strategy of using a different linker molecule for premodification. This approach offers a promising means of fine-tuning the coordination environment around atomically dispersed metal sites for precise control of catalytic performance.

Since PTRF-XAFS provides information only about the surrounding atoms of the absorbing atom, theoretical considerations were applied to create a more accurate modeling structure. To determine the entire structure of Cu adsorption of *o*-AA on TiO_2(110), various Cu adsorption configurations were modeled using density-functional theory (DFT) calculations, supporting the geometry investigations in Chapter 4.

Chapter 5 explores the synergy of experimental measurement (PTRF-EXAFS) and theoretical calculation (DFT) methods to enhance our understanding of atomic-scale resolution information. The proposed reconstructed structure for Cu dispersion on the TiO_2(110) aligns well with experimental data, emphasizing the significance of an integrated approach for precise structural determination. This study underscores the potential for advancements in comprehending complicated surface structures through the utilization of diverse approaches.

In my Ph.D. work, the preparation of Cu single-atom catalysts, typically challenging to obtain, was achieved through the premodification method. The 3D structure of the catalyst was successfully determined using the PTRF-XAFS technique. Beyond experimental limitations, a precise structure decision was facilitated through the

integration of theoretical approaches. This thesis contributes significantly to the atomic-level understanding of single-atom catalysts and provides a guideline for future SAC synthesis methods.

The structure determination method presented in this thesis, which integrates experimental and theoretical approaches, is still considered incomplete. It has been observed that structures determined solely through experimental methods and those reorganized based on theoretical considerations can both potentially exist. This suggests that pinpointing a single exact structure is highly challenging. However, employing computational chemical methods enables the presentation of structures with lower energy levels, facilitating more precise analysis of experimental data. By iteratively refining this process to narrow down the range of potential structures, it may eventually be possible to determine a singular structure.